The large-scale distribution of cool gas around luminous red galaxies

Guangtun Zhu, Brice Ménard, Dmitry Bizyaev, Howard Brewington, Garrett Ebelke, Shirley Ho, Karen Kinemuchi, Viktor Malanushenko, Elena Malanushenko, Moses Marchante, et al.

Monthly Notices
of the
ROYAL ASTRONOMICAL SOCIETY

MNRAS **439,** 3139–3155 (2014)
Advance Access publication 2014 February 24

doi:10.1093/mnras/stu186

The large-scale distribution of cool gas around luminous red galaxies

Guangtun Zhu,[1⋆] Brice Ménard,[1,2†] Dmitry Bizyaev,[3] Howard Brewington,[3] Garrett Ebelke,[3] Shirley Ho,[4] Karen Kinemuchi,[3] Viktor Malanushenko,[3] Elena Malanushenko,[3] Moses Marchante,[3] Surhud More,[2] Daniel Oravetz,[3] Kaike Pan,[3] Patrick Petitjean[5] and Audrey Simmons[3]

[1]*Department of Physics and Astronomy, Johns Hopkins University, 3400 N. Charles Street, Baltimore, MD 21218, USA*
[2]*Kavli IPMU (WPI), The University of Tokyo, Kashiwa 277-8583, Japan*
[3]*Apache Point Observatory and New Mexico State University, PO Box 59, Sunspot, NM 88349-0059, USA*
[4]*Bruce and Astrid McWilliams Center for Cosmology, Department of Physics, Carnegie Mellon University, 5000 Forbes Ave, Pittsburgh, PA 15213, USA*
[5]*Institut d'Astrophysique de Paris, UPMC-CNRS, UMR7095, 98bis Boulevard Arago, F-75014 Paris, France*

Accepted 2014 January 24. Received 2014 January 24; in original form 2013 September 12

ABSTRACT

We present a measurement of the correlation function between luminous red galaxies (LRGs) and cool gas traced by Mg II λλ2796, 2803 absorption, on scales ranging from about 30 kpc to 20 Mpc. The measurement is based on cross-correlating the positions of about one million red galaxies at $z \sim 0.5$ and the flux decrements induced in the spectra of about 10^5 background quasars from the Sloan Digital Sky Survey. We find that: (i) this galaxy–gas correlation reveals a change of slope on scales of about 1 Mpc, consistent with the expected transition from a dark matter halo dominated environment to a regime where clustering is dominated by halo–halo correlations. Assuming that, on average, the distribution of Mg II gas follows that of dark matter up to a gas-to-mass ratio, we find the standard halo model to provide an accurate description of the gas distribution over three orders of magnitude in scale. Within this framework, we estimate the average host halo mass of LRGs to be about $10^{13.5}$ $M_\odot$, in agreement with other methods. We also find the Mg II gas-to-mass ratio around LRGs to be consistent with the cosmic mean value estimated on Mpc scales. Combining our galaxy–gas correlation and the galaxy–mass correlation function from galaxy–galaxy lensing analyses, we can directly measure the Mg II gas-to-mass ratio as a function of scale and reach the same conclusion. (ii) From linewidth estimates, we show that the velocity dispersion of the gas clouds also shows the expected one- and two-halo behaviours. On large scales the gas distribution follows the Hubble flow, whereas on small scales we observe the velocity dispersion of the Mg II gas clouds to be lower than that of collisionless dark matter particles within their host halo.

Key words: intergalactic medium – quasars: absorption lines.

1 INTRODUCTION

Understanding the large-scale distribution of matter is a major goal in astrophysics. The advent of large photometric sky surveys combined with statistical analyses has allowed us to characterize the distribution of stars, dark matter and dust well beyond galactic discs. However, the large-scale distribution of gas and in particular gaseous metals which encodes key information about the cosmic baryon cycle remains poorly constrained.

Absorption line spectroscopy has been used for more than three decades to probe the distribution of gas around galaxies, the circumgalactic medium (CGM). Analyses have typically focused on the study of individual absorbers detected in the spectra of background quasars. While this approach has its merit, it is restricted to the study of strong absorbers and only allows us to probe the tip of the iceberg of the overall gas distribution. Probing the matter distribution on large scales where density is low requires a large range in sensitivity, which statistical analyses can often offer. Such statistical approaches have been successfully applied numerous times

⋆ E-mail: gz323@pha.jhu.edu
† Alfred P. Sloan Fellow.

to broad-band photometric surveys. However, statistical analyses aimed at probing the gaseous content of the CGM with spectroscopic data by extracting information below the noise level of individual spectra have been limited to a handful of analyses (Steidel et al. 2010; Bordoloi et al. 2011; Zhu & Ménard 2013b) constraining the gas distribution within a few hundred kpc around galaxies.

When measured over a broad range of scales, spatial correlation functions can provide us with valuable information on the distribution of matter within and beyond dark matter haloes. Obtaining such a measurement in the context of galaxy–gas correlations requires (i) a large number of foreground galaxies and background sources and (ii) the presence of an abundant species giving rise to a strong absorption feature. With existing data sets, maximizing those two criteria can be done by selecting luminous red galaxies (LRGs) from the Sloan Digital Sky survey (SDSS, York et al. 2000; Eisenstein et al. 2011) as foreground objects and measuring the associated Mg II absorption. In this paper, we present results of an analysis aimed at using these samples to measure the galaxy–gas correlation function over a broad range of scales. The measurement is based on a spatial cross-correlation between the position of about one million LRGs at $z \sim 0.5$ from SDSS and flux fluctuations induced in the spectra of background quasars by Mg II absorption lines. This measurement allows us to characterize the gaseous density profile on scales ranging from the inner dark matter halo of the galaxies up to more than 10 megaparsecs where the Hubble flow dominates the dynamics of galaxies.[1]

The paper proceeds as follows: we introduce the formalism of galaxy–gas correlation function in Section 2 and the data sets in Section 3. The measurements are presented in Section 4 and we discuss the results in the context of standard cold dark matter (CDM) paradigm in Section 5. Section 6 summarizes our findings. Throughout this work, we assume the ΛCDM cosmology with $(\Omega_{\rm m}, \Omega_\Lambda, h, \sigma_8, n_{\rm s}) = (0.3, 0.7, 0.7, 0.8, 0.96)$. The Roman subscript 'm' stands for all matter and unless stated otherwise scales are in physical units.

2 FORMALISM

The spherically averaged galaxy–gas spatial cross-correlation function is defined as

$$\xi_{\rm gal-gas}(r_{\rm 3D}) \equiv \langle \delta_{\rm gal}(r'_{\rm 3D}) \times \delta_{\rm gas}(r'_{\rm 3D} + r_{\rm 3D}) \rangle, \quad (1)$$

where δ is the density contrast, $\delta \equiv \rho/\overline{\rho} - 1$, and the ensemble average is performed over the entire survey volume. The projected cross-correlation function is given by

$$\omega_{\rm gal-gas}(r_{\rm p}) \equiv \langle \delta_{\rm gal}(r') \times \delta_{\rm gas}(r' + r_{\rm p}) \rangle, \quad (2)$$

where the 2D density contrast is defined as $\delta \equiv \Sigma/\overline{\Sigma} - 1$ and the surface density Σ is the integral of 3D density ρ along the line of sight over a redshift path of interest, and the ensemble average is performed over the entire survey area. When the galaxy field is discretized, i.e. when one considers only the positions of galaxy centres, the galaxy density contrast is given by a series of Dirac functions $\delta_D(r' - r'_i)$ at the position of each galaxy i. This restricts the ensemble average of the above equation to the positions of galaxies. The cross-correlation then reads

$$\omega_{\rm gal-gas}(r_{\rm p}) = \left\langle \frac{\Sigma^{\rm tot}_{\rm gas}(r_{\rm p}) - \overline{\Sigma}_{\rm gas}}{\overline{\Sigma}_{\rm gas}} \right\rangle_{\rm gal} . \quad (3)$$

The *total* mean gas surface density around galaxies can be expressed as

$$\langle \Sigma^{\rm tot}_{\rm gas}(r_{\rm p}) \rangle_{\rm gal} = \overline{\Sigma}_{\rm gas} \left[\omega_{\rm gal-gas}(r_{\rm p}) + 1 \right] . \quad (4)$$

In this work, we constrain the galaxy–gas correlation by measuring the *relative* gas absorption along quasar sightlines probing the vicinity of galaxies with respect to reference quasars. We are therefore not sensitive to the background value of the gas surface density and our analysis only allows us to measure the *excess* gas surface density around galaxies, $\Sigma_{\rm gas}$. This is given by

$$\langle \Sigma_{\rm gas}(r_{\rm p}) \rangle_{\rm gal} \equiv \overline{\Sigma}_{\rm gas}\, \omega_{\rm gal-gas}(r_{\rm p}) . \quad (5)$$

The projected surface gas density of a given species X is given by the product of its atomic mass m_X and column denstiy N

$$\Sigma_X = N \times m_X . \quad (6)$$

The absorption by atoms in the gas phase induces an optical depth $\tau(\lambda)$ given by

$$\tau(\lambda) = \frac{\pi e^2}{m_e c} f N \phi\left[\nu(\lambda)\right], \quad (7)$$

which is proportional to the column density N, oscillator strength f, and line profile $\phi(\nu)$. For a single-cloud system, the line profile follows the Voigt form determined by the transition wavelength λ_0, the intrinsic Lorentz width γ, the Doppler broadening factor b and the line-of-sight velocity V_0. For a single-cloud system, the centre-of-line optical depth is approximately

$$\tau_0 \simeq 1.5 \times 10^{-2} \frac{N f \lambda}{b}, \quad (8)$$

where N is in unit of $\rm cm^{-2}$, λ in Å, and b in $\rm kms^{-1}$. For a multicloud system, the line profile also depends on the number of clouds and their velocity spread. The optical depth causes a flux decrement in the background source spectrum given by

$$R(\lambda) \equiv \frac{F(\lambda)}{\hat{F}_{\rm cont}(\lambda)} = {\rm e}^{-\tau(\lambda)}, \quad (9)$$

where $F(\lambda)$ is the observed spectrum and $\hat{F}_{\rm cont}(\lambda)$ is the intrinsic continuum of the background source. From an observational point of view, we quantify the optical depth by measuring the absorption rest equivalent width W_0, obtained by integrating the flux decrement over the absorption line profile defined by $\phi(\lambda)$,

$$W_0 \equiv \int [1 - {\rm e}^{-\tau(\lambda)}]\, {\rm d}\lambda$$
$$= \int [1 - R(\lambda)]\, {\rm d}\lambda. \quad (10)$$

If the optical depth at the line centre is smaller than unity, the column density is simply given by

$$N = 1.13 \times 10^{20}\, {\rm cm^{-2}} \frac{W_0}{f \lambda^2}, \quad (11)$$

where both W_0 and λ are in unit of Å.

The above equations show that the projected galaxy–gas correlation function can be constrained by measuring the correlation

[1] In an independent analysis, Pérez-Ràfols et al. (in preparation) also detect the galaxy–Mg II absorption correlation up to Mpc scales with similar amplitude. The authors use this signal to estimate the cosmic opacity due to Mg II absorption.

between galaxy positions and the rest equivalent width induced by its surrounding gas distribution

$$\langle W_0\rangle_{\rm gal}(r_{\rm p}) \equiv \langle \delta_{\rm gal}(r) \times\ W_0(r+r_{\rm p})\rangle$$
$$= \int [1-\langle R(\lambda, r_p)\rangle_{\rm gal}]\,{\rm d}\lambda. \quad (12)$$

In the next sections, we will present a measurement of $\langle W_0\rangle_{\rm gal}(r_{\rm p})$ for Mg II absorption induced by gas around LRGs. In the rest of the paper, all scale-dependent ensemble averages will be taken around galaxies. For clarity we will drop the subscript 'gal' in the formalism.

Several authors have investigated galaxy–*absorber* correlations which correspond to the cross-correlation between galaxies and individually detected absorbers, some of them explicitly in the context of LRGs and Mg II (e.g. Bouché, Murphy & Péroux 2004; Gauthier, Chen & Tinker 2009; Lundgren et al. 2009, 2011), which is a valuable tool to shed light on the connection between gas and galaxies. We note that the galaxy–gas correlation introduced above is distinctively different from galaxy–absorber correlations. The galaxy–gas correlation probes the mean of the *entire* gas distribution around galaxies, while galaxy–absorber correlations only probe the distribution of gas clouds for which the equivalent width is directly detectable and usually selected to be above a given threshold. The latter is therefore only sensitive to a fraction of the gas distribution.

3 DATA ANALYSIS

Our goal is to constrain the galaxy–gas (metal) correlation function over a broad range of scales. Doing so requires (i) a large number of foreground galaxies and background sources and (ii) the presence of an abundant species giving rise to a strong absorption feature. With existing data sets, maximizing those two criteria is done by selecting LRGs from the SDSS as foreground objects and measuring the associated Mg II absorption.

3.1 Mg II absorption lines

The Mg II λλ2796, 2803 doublet has played a major role in gas astrophysics because of their strength and their location in the visible part of the spectrum. They correspond to the fine structure splitting of the singly ionized magnesium excited states Mg II (Mg^+). Being an abundant element, $\log({\rm Mg/H})_\odot + 12 \simeq 7.6$ (Asplund et al. 2009), it is found in a range of astrophysical environments. Magnesium is a moderately refractory element and has ionization potentials of 7.65 and 15.04 eV, for Mg I and Mg II, respectively (Morton 2003). At redshift greater than about 0.3, the Mg II λλ2796, 2803 lines are the strongest absorption lines of 10^4 K gas accessible to ground-based observations. The Mg II doublet has been used for three decades to study the intergalactic medium. It is the lines used in the observational discovery of the CGM (Bergeron 1986) and has been used extensively since then (e.g. Steidel & Sargent 1992; Churchill et al. 1999; Nestor, Turnshek & Rao 2005; Narayanan et al. 2007, among others).

The oscillator strength of the two lines are 0.608 and 0.303 for Mg II λλ2796, 2803 (Kelleher & Podobedova 2008). When both lines are saturated, their line ratio is 1, and when neither is saturated, the line ratio is 2. For a thermal broadening factor b about 4 $\rm kms^{-1}$ (corresponding to about 25 000 K, e.g. Churchill et al. 2000), saturation begins for an Mg II column density of about $10^{12.5}$ $\rm cm^{-2}$, which occurs at a total rest equivalent width ($W_0^{\rm Mg\,II}$, sum of the two lines) of about 0.15 Å.

3.2 Samples and analysis

The sample of LRGs used in this work originates from the eleventh Data Release (DR11[2]) of SDSS. It includes about one million LRGs from the Baryonic Oscillation Spectroscopic Survey (BOSS; Dawson et al. 2013) with mean stellar mass $\langle M_*\rangle \sim 10^{11.5}\,{\rm M}_\odot$ (e.g. Chen et al. 2012) and redshift $\langle z\rangle \sim 0.57$. The photometric and spectroscopic data were obtained with the wide-field imaging camera (Gunn et al. 1998) and the new multi-object spectrographs (Smee et al. 2013) on the SDSS telescope (Gunn et al. 2006). From this parent sample, we select 849 533 galaxies at $0.4 < z < 0.75$ where Mg II is accessible in the optical. We do not have additional selection requirement other than the redshift cut and therefore almost all the galaxies are optically luminous and red.

We measure the absorption induced by the gas around these galaxies in the spectra of background quasars. We use spectra from the Data Release 7 (DR7, Abazajian et al. 2009; Schneider et al. 2010) of SDSS I-II and the improved redshift estimates by Hewett & Wild (2010). The sample includes 107 194 quasars at $0.1 < z < 6.5$.

Accurate estimation of the source flux continuum $\hat{F}(\lambda)$ (equation 9) is crucial to detect absorption features. We use the method presented in Zhu & Ménard (2013a), applied to the 84 533 quasars with $z < 4.7$. In a nutshell, this method employs the robust dimensionality-reduction technique *non-negative matrix factorization* (NMF; Lee & Seung 1999; Blanton & Roweis 2007) to construct a basis set of non-negative quasar eigenspectra, and fits each observed quasar spectrum with a non-negative linear combination of these eigenspectra. Large-scale residuals not accounted for by the NMF basis set are removed with appropriate median filters. The smallest width of such filters has to be kept significantly larger than the size of the absorption feature we are interested in. This set of flux residuals has been used to create a sample of about 50 000 absorber systems (Zhu & Ménard 2013a) and to measure the total amount of Ca II around low-redshift galaxies (Zhu & Ménard 2013b). In the present analysis, we use only quasars for which $z_{\rm quasar} - z_{\rm LRG} > 0.1$. The median stellar mass and redshift of LRGs in the LRG–quasar pairs are $\langle M_*\rangle = 10^{11.4}\,{\rm M}_\odot$ and $\langle z\rangle \simeq 0.52$. The set of flux residuals obtained this way allows us to construct composite residuals consistent with unity at the one percent level. To further improve the accuracy and remove systematic trends, we apply our procedure to a set of LRG–quasar pairs for which the quasars are selected to have the same redshift distribution as the original sample but are randomly selected over the sky. This is used to map out large-scale, sub-percent systematic shifts in the mean residuals which are then subtracted when analysing a given sample. This step is required to properly estimate the zero-point of the mean flux residuals over a broad wavelength range.

To quantify the rest equivalent width of the absorption of the Mg II λλ2796, 2803 doublet, we perform a double-Gaussian fit of the absorption feature expected at the redshift of the galaxy, allowing the width and line ratio to be free parameters. Absorption being a multiplicative effect, we estimate the ensemble average using a geometric mean. This provides us with an estimate of the arithmetic mean of the corresponding optical depth. However, we note that using an arithmetic mean yields similar results, as expected when measuring weak absorption lines. Our estimator is inverse-variance weighted, using the wavelength-dependent noise given by

[2] DR11 will be released in 2014 December. Here, we use the redshift catalogue based on version v5_6_0 of the reduction pipeline (Bolton et al. 2012).

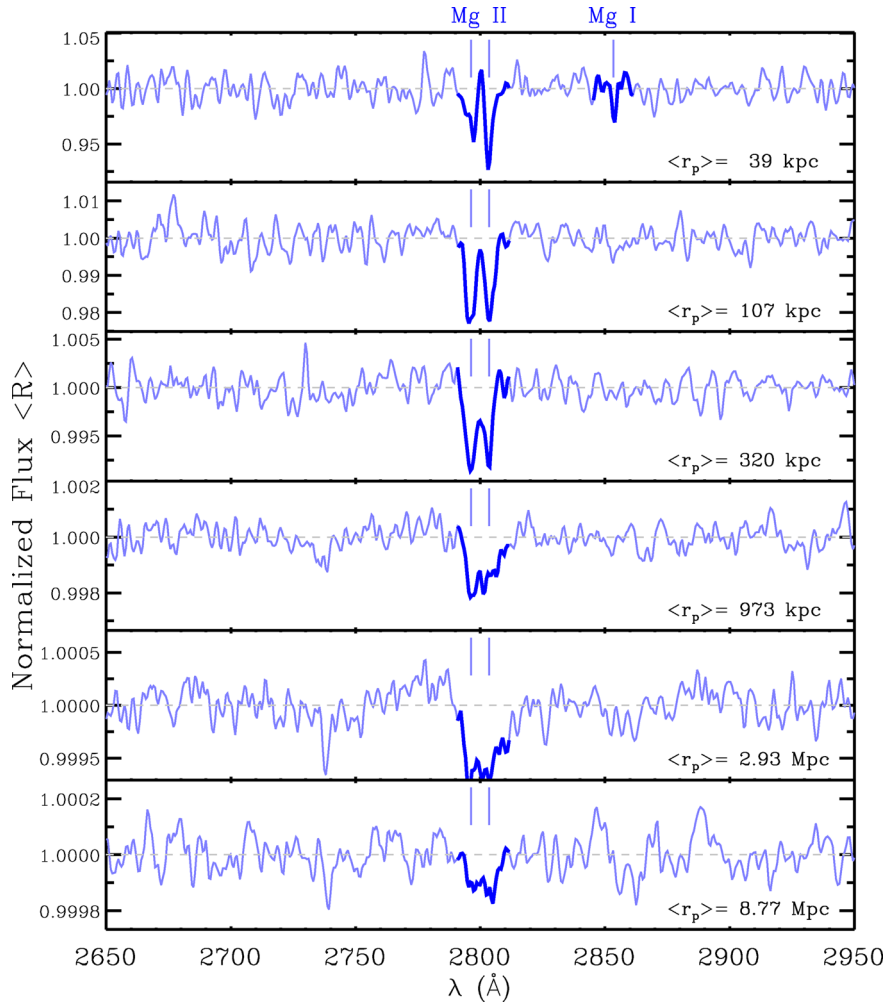

Figure 1. Examples of stacked continuum-normalized spectra of background quasars as a function of impact parameter (projected galactocentric distance) from foreground luminous red galaxies (LRGs) at $z \sim 0.5$. The vertical ticks and dark blue colours mark the expected positions of Mg II λλ2796, 2803 and Mg I λ2853.

the SDSS pipeline. Throughout the paper, we will present the total rest equivalent width of the doublet instead of just one of the two lines.

4 RESULTS

4.1 The galaxy–gas correlation

We measure the spatial cross-correlation between the position of our selected sample of LRGs and the Mg II rest equivalent width induced in the spectra of background quasars, as a function of scale, $\langle W_0^{\rm Mg\,II}\rangle(r_{\rm p})$ (see equation 12). Fig. 1 presents examples of the intermediate products of the analysis, the stacked continuum-normalized spectra $\langle R(\lambda)\rangle$. The figure highlights the expected positions of Mg II λλ2796, 2803 and Mg I λ2803 with vertical tick marks and dark blue colour. Note that the absorption scale varies from about 10^{-2} at the top to about 10^{-4} at the bottom. In Table 1 and Fig. 2, we present the mean Mg II rest equivalent width $\langle W_0\rangle$ (including the contribution from both absorption lines) with solid circles between 30 kpc and 20 Mpc. We estimate the rest equivalent width errors by bootstrapping the sample of LRG-quasar pairs one hundred times.

To validate the robustness of these measurements, we perform two null hypothesis tests: (1) we measure the mean rest equivalent

Table 1. The LRG–Mg II correlation at $z \sim 0.5$.

$r_{\rm p}$ bin (Mpc)	Median $r_{\rm p}$ (Mpc)	$N_{\rm pairs}$	$\langle W_0^{\rm Mg\,II}\rangle^a$ (mÅ)	$\sigma(\langle W_0^{\rm Mg\,II}\rangle)^b$ (mÅ)
(0.030, 0.045]^c	0.039	35	494.71	145.21
(0.045, 0.068]	0.056	88	352.58	78.68
(0.067, 0.101]	0.086	200	267.94	40.05
(0.101, 0.152]	0.128	434	161.29	34.91
(0.152, 0.228]	0.191	880	102.67	19.76
(0.228, 0.342]	0.289	1936	86.60	11.49
(0.342, 0.513]	0.432	3964	33.95	10.10
(0.513, 0.769]	0.648	8911	35.42	6.11
(0.769, 1.153]	0.974	19981	16.54	4.59
(1.153, 1.730]	1.461	45030	14.06	2.20
(1.730, 2.595]	2.192	101153	11.01	1.94
(2.595, 3.892]	3.287	228261	8.17	1.32
(3.892, 5.839]	4.929	512263	5.00	0.77
(5.839, 8.758]	7.395	1151523	5.23	1.03
(8.758, 13.137]	11.092	2591671	3.04	0.63
(13.137, 18.000]	15.694	4086471	2.51	0.57

[a]Mean rest equivalent width of Mg II (sum of two lines).
[b]Bootstrapping errors of $\langle W_0^{\rm Mg\,II}\rangle$.
[c]Mg I measurement in this bin: $\langle W_0^{\rm Mg\,I}\rangle = 83 \pm 64$ mÅ.

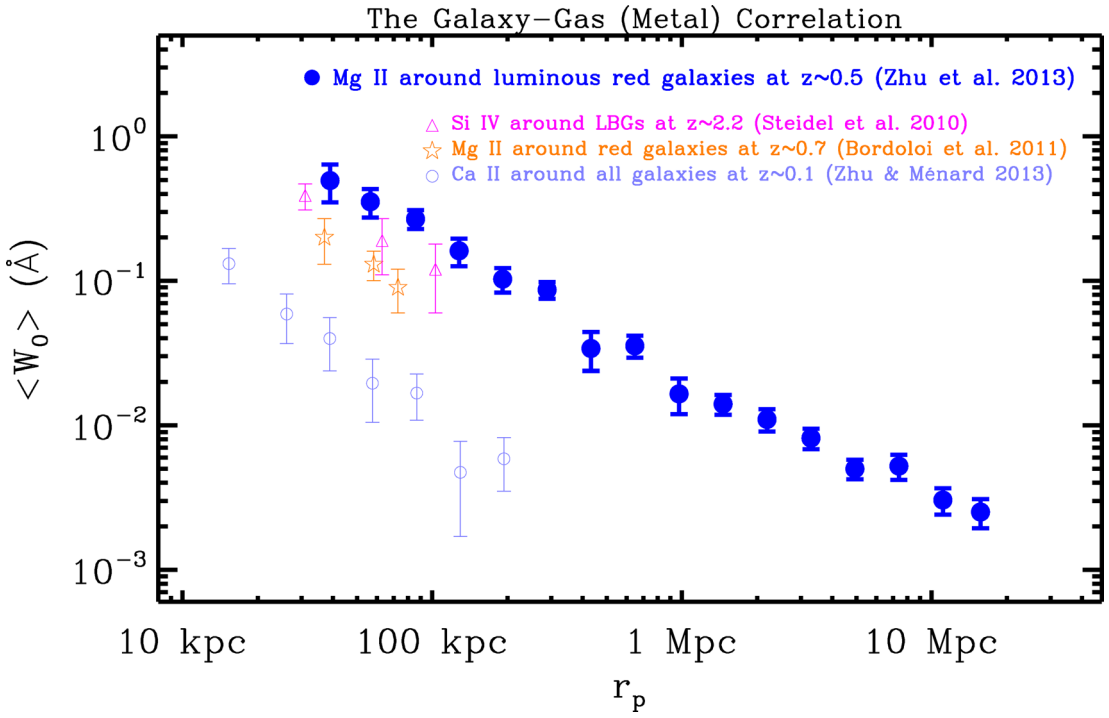

Figure 2. Mean gas absorption profiles (in terms of rest equivalent widths) as a function of scale. The blue solid circles represent our measurements of the LRG–Mg II correlation function at $z \sim 0.5$ (here the quoted rest equivalent width corresponds to the sum of the two lines λλ2796, 2803). It is detected from about 30 kpc to 20 Mpc. Other symbols show measurements of several metal species around different types of galaxies from the literature (see the text).

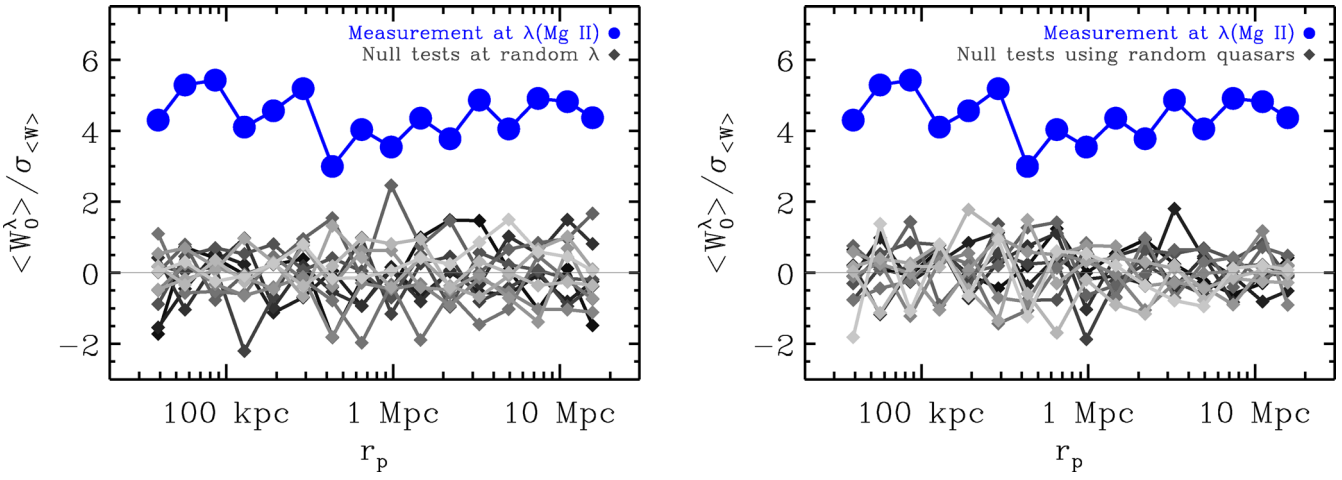

Figure 3. Null hypothesis tests for the robustness of the Mg II detection. Left panel: significance of rest equivalent width measurements at randomly selected wavelengths. Right panel: significance of rest equivalent width measurements using random quasars at the same redshifts as those in galaxy–quasar pairs. The blue solid circles show the significance of the Mg II absorption measurements.

width at randomly chosen wavelengths; and (2) we measure the expected Mg II rest equivalent width not using the corresponding background quasars located in the vicinity of foreground LRGs but instead random quasars with similar redshifts. In both cases, we fix the width of the Gaussian line profile to be roughly the same as that of the actual measurement, in this case four pixels. The results of these null tests are shown in Fig. 3. Each panel shows the measurements for 12 random realizations (grey diamonds). In both cases, the null test measurements are consistent with random noise and indicate that the detection of Mg II absorption shown in Table 1 and Fig. 2 is robust and not induced by systematic effects. These tests can also be used to estimate the intrinsic noise level of the statistical measurement.

To put our results in context, we first present existing measurements of the galaxy–metal absorption correlations for several species from the literature. This compilation is shown with open symbols in Fig. 2. The magenta triangles are measurements for the Si IV λ1393 around Lyman-break galaxies (LBGs) at $z \sim 2.2$ by Steidel et al. (2010), who also reported measurements for Lyα, Si II λ1260, C II λ1334, Si II λ1526, C IV λ1549 and Al II λ1670 on similar scales (not shown to avoid crowdedness). Bordoloi et al. (2011) measured the mean Mg II absorption around different types

of galaxies at $z \sim 0.7$. The orange stars show their measurements around red massive galaxies with stellar mass $M_* > 10^{10.7}\,\mathrm{M}_\odot$ (though still about 0.5 dex less massive than the LRGs used in this study). The grey circles show the mean Ca II absorption around all galaxies at $z \sim 0.1$ measured by Zhu & Ménard (2013b). Note this compilation is inhomogeneous in terms of galaxy types and redshifts but it shows the range of scales accessible to previous studies. The present analysis extends the detectability of the galaxy–gas (metal) correlation function up to about 20 Mpc, i.e. by two orders of magnitude.

The mean absorption profile does not show any cut-off scale. The spatial correlation roughly follows a power-law form of $r_\mathrm{p}^{-1.5}$. Such a slope implies a roughly constant S/N across all scales as the decrease in the signal amplitude is compensated by an increase in the number of usable pairs. This property allows measurements of two-point correlation functions to reach large scales, such as in galaxy clustering and galaxy–galaxy lensing analyses. Our measurement allows us to probe the gas distribution around galaxies below and above the virial radius simultaneously. In Section 5, we will interpret these measurements in the context of the standard CDM model.

4.2 From equivalent width to column density

To estimate the surface density of magnesium from our mean measurements, we use the weaker of the two Mg II lines. From a measurement of the rest equivalent width of the full doublet, we estimate

$$\langle W_0^{\lambda 2803}\rangle = \frac{\langle W_0^{\mathrm{Mg\,II}}\rangle}{1+DR}, \tag{13}$$

where DR is the doublet ratio, bound between 1 and 2.

When absorption lines are not saturated we can directly infer gas column densities, as shown in equation (11). The saturation level depends on the column density and thermal broadening factor b. From high-resolution spectroscopic studies the thermal broadening factor of Mg II gas appears to be of the order of several kms^{-1} (e.g. Churchill et al. 2000). Taking b to be $4\,\mathrm{kms}^{-1}$, corresponding to 25 000 K, the stronger of the two Mg II lines starts to saturate when $W_0^{\mathrm{Mg\,II}} \gtrsim 0.15$ Å.

In the unsaturated regime, the Mg II surface density is given by (see equation 11)

$$\langle \hat{\Sigma}_{\mathrm{Mg\,II}}\rangle = \frac{1.13\times 10^{20}\, m_{\mathrm{Mg}}}{f_{2803}\,\lambda^2}\,\langle W_0^{\lambda 2803}\rangle \mathrm{cm}^{-2}, \tag{14}$$

where m_{Mg} is the atomic mass of magnesium.

On scales greater than about 200 kpc, our measurements show that $\langle W_0^{\mathrm{Mg\,II}}\rangle < 0.1$ Å. In addition, our estimators show that the mean and median values are similar. This indicates that the fraction of saturated systems contributing to the overall signal is negligible. In this regime, we therefore expect a line ratio close to 2. This is in rough agreement with line ratio estimates of our stacked residual spectra, as shown in Fig. 4. We note that the estimation of the line ratio of weak lines, detected a few orders-of-magnitude below the noise level of individual spectra, is difficult and possibly subject to systematic effects. Such line ratio estimates involve measuring changes in the second-order moment of the (weak) stacked line profiles, as opposed to the rest equivalent width estimation which is based on the zeroth-order moment of the line profile. It is therefore not surprising that the scatter of the measured line ratios is large.

Some authors have reported that in some cases weak absorbers with $W_0^{\mathrm{Mg\,II}} < 0.15$ Å can have line ratios smaller than 2, indicating

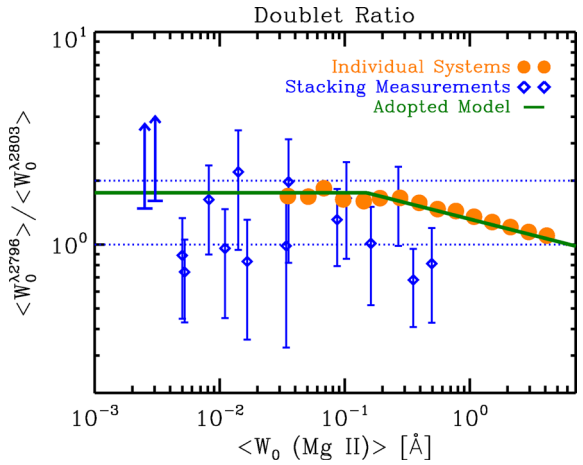

Figure 4. Doublet ratios as a function of $W_0^{\mathrm{Mg\,II}}$. The orange points are median values of individual Mg II absorbers from Churchill et al. (1999) and Zhu & Ménard (2013a), and the green line is our adopted formula to capture the dependence on $W_0^{\mathrm{Mg\,II}}$. The blue points are the measurements from the statistical analysis in this work. The two measurements on the far left are 2σ lower limits because the double-Gaussian fitting gives too small values of $\langle W_0^{\lambda 2803}\rangle$.

the strong line can still be saturated (e.g. Churchill et al. 2000). We can obtain some guidance on the expected line ratio from direct detections of Mg II absorber systems. Using the individual absorber systems from Churchill et al. (1999) and Zhu & Ménard (2013a), we compute the median line ratio as a function of $W_0^{\mathrm{Mg\,II}}$. This is shown with orange point in Fig. 4. As expected we observe a break at around $W_0^{\mathrm{Mg\,II}} \simeq 0.15$Å, below which the mean line ratio appears to be constant, with a value of about 1.75. The similarity between the mean and the median ($\langle W_0^{\mathrm{Mg\,II}}\rangle$) as a function of scale suggests that the fraction of saturated systems is scale independent. We therefore expect that the overall gas absorption is dominated by weak systems and $\langle \hat{\Sigma}_{\mathrm{Mg\,II}}\rangle \simeq \langle \Sigma^{\mathrm{tot}}_{\mathrm{Mg\,II}}\rangle$.

At $W_0^{\mathrm{Mg\,II}} \gtrsim 0.15$ Å, a higher fraction of absorber systems is expected to occur. As can be seen in Fig. 4, the median line ratio obtained from direct detections of absorbers reveals such a trend. To capture this behaviour, we adopt the following formula for absorbers in this regime:

$$\log_{10} DR = -0.15\,\log_{10}\frac{\langle W_0^{\mathrm{Mg\,II}}\rangle}{0.15\,\text{Å}} + \log_{10} 1.75, \tag{15}$$

which is shown with the green line in the figure. In this regime, we estimate the Mg II surface density estimator using equation (14) with the line ratio provided by the above relation. On the corresponding scales, i.e. at $r_p < 200$ kpc, the fraction of saturated systems is expected to increase compared to that on larger scales. Our surface density estimate is therefore a *minimum* value of the total surface density. In Appendix B, we investigate the effect of different line ratio treatments and show that our conclusions are not strongly affected by this consideration.

4.3 The velocity-space galaxy–gas correlation

The galaxy–gas correlation function is the projected surface density integrated along the line of sight, i.e. in the redshift (velocity) space. The velocity width of the absorption lines measured in the statistical analysis provides dynamical information of gas clouds

around galaxies. The mean absorption line includes contributions from a large number of clouds and its width reflects the velocity dispersion of these clouds.

We present the velocity dispersion of Mg II gas clouds in Fig. 8, measured from the double-Gaussian profile fitting. The errorbars are again obtained from bootstrapping. The velocity dispersion of Mg II gas clouds increases from about 100 $\mathrm{km\,s^{-1}}$ at 30 kpc to about 700 $\mathrm{km\,s^{-1}}$ at 20 Mpc. This is consistent with theoretical expectations. On small scales, the gas clouds are mostly from the LRG host haloes and the velocity dispersion reflects their motion within the halo, while on larger scales, the gas clouds reside in neighbouring dark matter haloes and the velocity dispersion is determined by the motion of the neighbouring haloes, including the Hubble flow due to the expansion of the universe. We will discuss the measurements in more detail in the CDM cosmological context in Section 5.3.

5 INTERPRETATION

5.1 The galaxy–gas correlation with the halo model

We now model the observed LRG–Mg II correlation function. The measurement presented in Fig. 2 shows the mean Mg II rest equivalent width as a function of impact parameter, ranging from about 30 kpc, where most of the gas is expected to lie within the host dark matter halo of the LRGs, to several megaparsecs where most of the gas is expected to be associated with galaxies in neighbouring haloes. To describe the gas distribution over the entire range of scales, we make use of the dark matter halo model, originally developed to model the galaxy–mass and galaxy–galaxy correlation functions (for a review, see Cooray & Sheth 2002).

The dark matter halo model assumes that halo properties, such as density profile, abundance and galaxy occupation, are determined solely by the halo mass. Here, we extend this assumption to the gas distribution: we consider the gas-to-mass ratio $f_{\rm gas}$ to depend only on halo mass. This implies that, on average, the gas density profile in a halo with virial mass M has the same NFW shape as dark matter up to an overall normalization determined by $f_{\rm gas}(M)$. The halo model we use has three parameters:

(i) the average virial mass $M_{\rm halo}$,
(ii) the gas-to-mass ratio $f_{\rm gas}^{\rm 1h}(M_{\rm halo})$ of the host dark matter haloes (the one-halo term),
(iii) the mean gas-to-mass ratio $f_{\rm gas}^{\rm 2h}$ in the CGM of all galaxies at $z \sim 0.5$ (the two-halo term).

In this framework, the mean gas surface density around galaxies is given by

$$\Sigma_{\rm gas}(r_{\rm p}) = f_{\rm gas}^{\rm 1h}(M_{\rm halo})\Sigma_{\rm m}^{\rm 1h}(r_{\rm p}|M_{\rm halo}) + f_{\rm gas}^{\rm 2h}\Sigma_{\rm m}^{\rm 2h}(r_{\rm p}|M_{\rm halo}), \quad (16)$$

where the one-halo term of the total surface density $\Sigma_{\rm m}^{\rm 1h}(r_{\rm p}|M_{\rm halo})$ is obtained by integrating the 3D NFW density profile along the line of sight and the two-halo term $\Sigma_{\rm m}^{\rm 2h}(r_{\rm p}|M_{\rm halo})$ is calculated through the halo-mass cross-correlation. Note that for simplicity we have dropped the ensemble average symbol. It is also worth emphasizing that the two-halo term $f_{\rm gas}^{\rm 2h}$ is the mean value over all neighbouring haloes, which can have a wide range of gas-to-mass ratios. Galaxies can be central or satellite systems within a dark matter halo. LRGs being the most massive galaxies in the universe, we further assume all of them are central galaxies and the average mass of their host haloes is $M_{\rm halo}$. We have tested that if a small fraction (∼10 per cent) of LRGs are satellite systems, our conclusions on the galaxy–gas and the galaxy–mass correlations below are not affected, unless the gas-to-mass ratio of the host haloes of these satellite LRGs are orders-of-magnitude higher than other haloes. We present a detailed prescription of our halo model in Appendix A.

The halo model describes the mean projected surface density. As described in Section 4.2, we adopt 1.75 for the line ratio when $\langle W_0^{\rm Mg\,II}\rangle < 0.15$ Å and equation (15) otherwise, as suggested by individual systems. We then estimate the weaker line (λ2803) strength and the Mg II column density applying the linear relation of the curve of growth, equation (11).

We generate Monte Carlo simulations spanning the three-parameter ($M_{\rm halo}$, $f_{\rm Mg\,II}^{\rm 1h}$, $f_{\rm Mg\,II}^{\rm 2h}$) space and find the best fitting model to be

$$\log_{10} M_{\rm halo}/{\rm M}_\odot = 13.5^{+0.3}_{-0.3} \quad (17)$$

$$\log_{10} f_{\rm Mg\,II}^{\rm 1h} = -8.3^{+0.2}_{-0.2} \quad (18)$$

$$\log_{10} f_{\rm Mg\,II}^{\rm 2h} = -8.1^{+0.1}_{-0.1}. \quad (19)$$

The reduced chi-square is $\chi^2/{\rm d.o.f.} = 0.72$. The errors reflect 1σ confidence level and do not include uncertainties in the conversion from rest equivalent width to column density, which we present separately in Appendix B. Fig. 5 shows the best fitting halo model and the fractional residuals. The small residuals show how well this halo model with only three parameters fits the data across about three orders of magnitude in scale. In Fig. 6, we show the joint likelihood distributions in the $M_{\rm halo} - f_{\rm Mg\,II}^{\rm 1h}$ (green) and the $M_{\rm halo} - f_{\rm Mg\,II}^{\rm 2h}$ (orange) sub-spaces. The halo mass and gas-to-mass ratios are degenerate because they affect the overall amplitude in the same direction.

The best fitting halo mass of LRGs is in excellent agreement with constraints from the halo modelling of the LRG–LRG autocorrelation by White et al. (2011), who estimated the mean halo mass of BOSS LRGs to be about $2{-}4 \times 10^{13}\,{\rm M}_\odot$. Galaxy–galaxy lensing analyses for the BOSS LRG sample are not yet available. We therefore choose to compare our results to the findings of Mandelbaum et al. (2006) who used a sample of LRGs at redshift $z \sim 0.2$ (red sub-sample 6). This sample has a similar average stellar mass and number density as the BOSS LRGs and the host halo mass is also consistent with that obtained from the LRG–LRG correlation by White et al. (2011). The best fitting halo mass of this sample is $(2.3 \pm 0.6) \times 10^{13}\,{\rm M}_\odot$, shown with the vertical grey band in Fig. 6. The excellent agreement between the constraints from different correlations shows our dark matter–gas halo model, with the assumption that gas shares the same density profile as dark matter, works well in describing the cool gas distribution in the cosmological context.

5.2 Gas-to-mass ratio from observations

Having showed that the halo model applied to the gas distribution around LRGs provides us with a halo-mass estimate consistent with what is found with other methods, we now focus on the value of the Mg II gas-to-mass ratio inferred from the same fit and assumption that on average the distribution of Mg II gas follows that of dark matter.

To constrain the gas distribution with respect to mass from observations in a model-independent way, we can simply divide the observed galaxy–gas correlation (the projected gas density profile), in our case the observed LRG–Mg II correlation, by the observed galaxy–mass correlation (the projected mass density profile). To do so, we use again the red sub-sample 6 at redshift $z \sim 0.2$ in

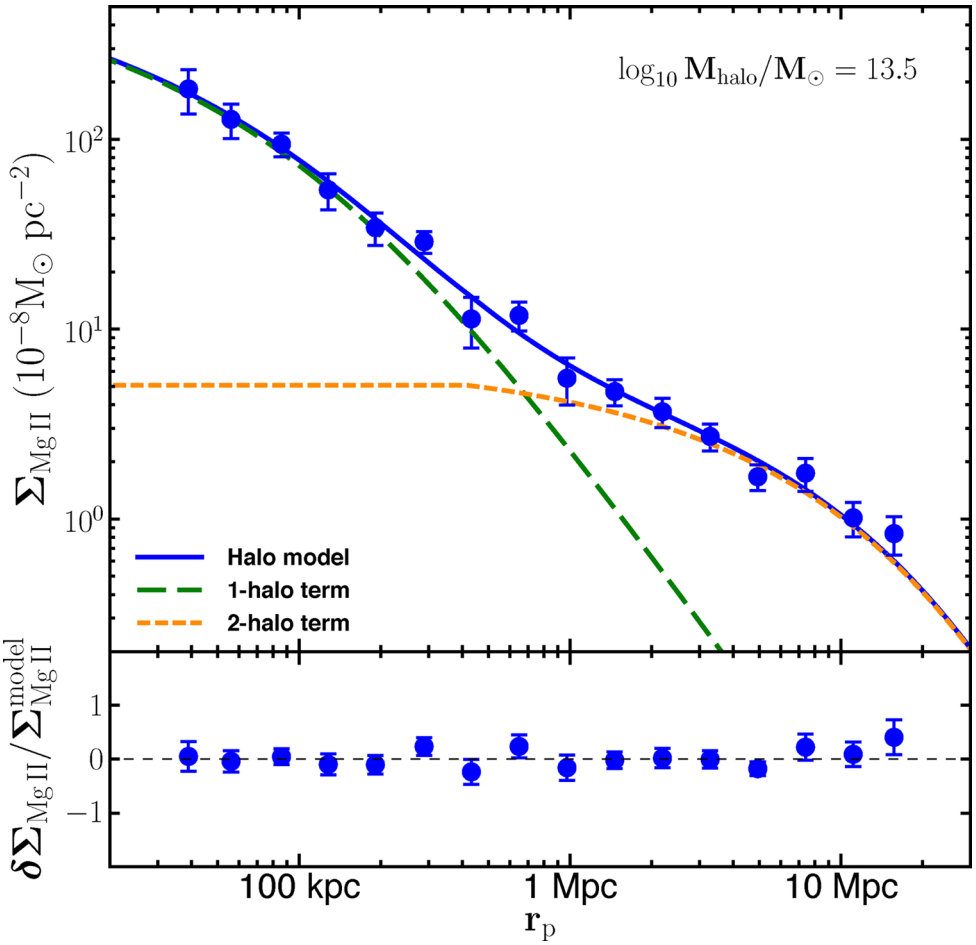

Figure 5. The best fitting halo model. Upper panel shows the best fitting halo model, decomposed into one-halo and two-halo terms. Lower panel shows the fractional residuals. The halo model has three parameters: average LRG host halo mass $M_{\rm halo}$, Mg II gas-to-mass ratio in the host halo $f^{\rm 1h}_{\rm Mg\,II}$, and mean Mg II gas-to-mass ratio of all galaxies $f^{\rm 2h}_{\rm Mg\,II}$.

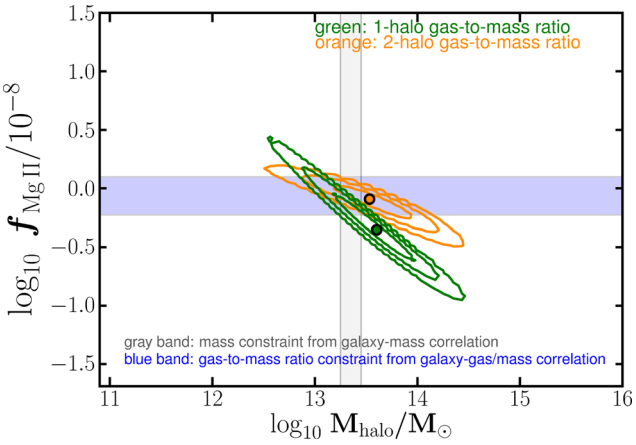

Figure 6. Joint likelihood distributions for halo mass and gas-to-mass ratios. The contours indicate 1σ (68.3 per cent), 2σ (95.4 per cent), and 3σ (99.7 per cent) confidence intervals.

Mandelbaum et al. (2006). The observations are presented in the top and middle panels of Fig. 7. Galaxy–galaxy lensing analyses probe the difference between the average surface density within a radius and the surface density at that radius: $\Delta\Sigma_{\rm m}(r_{\rm p}) = \Sigma_{\rm m}(<r_{\rm p}) - \Sigma_{\rm m}(r_{\rm p})$. For a direct comparison, we estimate the average surface density within an aperture $\Sigma_{\rm m}(<r_{\rm p})$ using their best fitting halo model and subtract the observable $\Delta\Sigma_{\rm m}(r_{\rm p})$ from it. The halo model is overlaid in the middle panel. As done previously, we ignore the effect of satellite systems. Because the impact parameter binning is different, we use the best fitting halo model for interpolation to estimate the projected surface density at a given impact parameter $\Sigma_{\rm m}(r_{\rm p})$.[3] Since the LRG–mass correlation is measured at $z \sim 0.2$, we also evolved the measurements to $z = 0.52$ under the adopted cosmology.

We present the observed Mg II gas-to-mass ratio around LRGs as a function of impact parameter in the bottom panel of Fig. 7, where we have overplotted a horizontal light blue band to encompass the maximum and minimum value. We find the mean Mg II-to-mass ratio to depend only weakly on scale. It varies by roughly a factor of 2 over three orders of magnitude in radius. This range of Mg II-to-mass ratio is also shown in Fig. 6 as a blue region. We find it to be consistent with the constraints obtained from the halo model of the galaxy–gas correlation. Having applied the halo model to the gas distribution and found halo mass and gas-to-mass ratios in agreement with other methods suggests that it might be possible

[3] We note that, using magnification instead of shear would allow us to directly infer the surface density $\Sigma_{\rm m}$ rather than $\Delta\Sigma_{\rm m}$, and interpolation with the halo model would not be necessary.

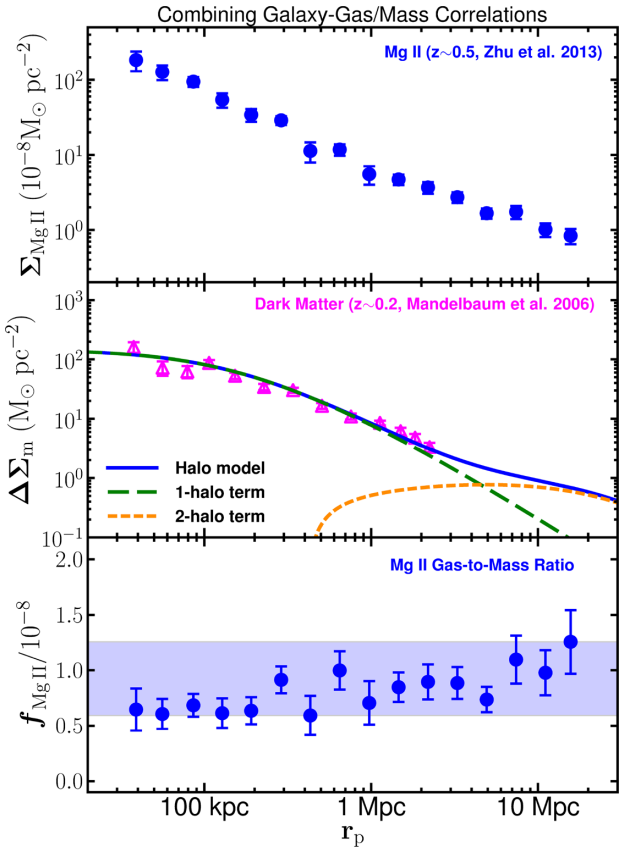

Figure 7. Direct constraints on the Mg II gas-to-mass ratio: the top panel shows the LRG–Mg II correlation function at $z \sim 0.5$, the middle one shows the LRG–mass correlation by Mandelbaum et al. (2006) at $z \sim 0.2$ from galaxy–galaxy lensing, with the lines showing the halo model with their best fitting halo mass $10^{13.4}$ M$_\odot$. The lower panel shows the ratio between these two quantities and provides us with a measurement of the Mg II gas-to-mass ratio as a function of impact parameter.

to apply the halo model to galaxy–gas correlations to constrain the mass of dark matter haloes.

We can now put strong constraints on the Mg II gas-to-mass ratio around LRGs, with consistent results from the halo modelling of the galaxy–gas correlation function itself, and the combination of the observed galaxy–gas and galaxy–mass correlations. We can conclude that, in the LRG host haloes at redshift 0.5, (i) the Mg II gas-to-mass ratio is scale independent, i.e. the average Mg II gas density profile follows the same NFW shape as dark matter; and (ii) the Mg II gas-to-mass ratio is the same as the cosmic value within errors, which is about 10^{-8}.

We first examine the measured value of the Mg II gas-to-mass ratio. We emphasize that on large scales, the two-halo term $f^{\rm 2h}_{\rm Mg\,II}$ is the mean value in the CGM of *all* galaxies in the universe at redshift 0.5. Neglecting the possible evolution of Mg II abundance from redshift 0.5 to present day, the value of 10^{-8} indicates

$$\Omega^{\rm CGM}_{\rm Mg\,II} = \Omega_{\rm m} \times f^{\rm 2h}_{\rm Mg\,II} \approx 3 \times 10^{-9}. \quad (20)$$

Taking the solar abundance of Mg ([Mg/H] $= 4 \times 10^{-5}$) as the maximum, this means Mg II probes at least 10^{-4} of total baryons in the universe. If the mean Mg II abundance is only 0.1 solar, as in High-Velocity Clouds/Magellanic Stream, then it traces about $10^{-3} \times (0.1/[{\rm Mg\,II/H}])$ of total baryons. In the one-halo regime, the Mg II-to-mass ratio in the LRG host haloes is the same as the cosmic value. Assuming 0.1 solar abundance again, the cool gas traced by Mg II in the LRG host haloes would be about 10^{10}–10^{11} M$_\odot$, much more than their interstellar gas content (about 10^9 M$_\odot$, e.g. Oosterloo et al. 2010; Young et al. 2011).

5.3 The gas cloud velocity dispersion with the halo model

The velocity width of the mean absorption lines provides dynamical information of gas clouds around galaxies. We present the line-of-sight velocity dispersion measurements in Fig. 8. The velocity

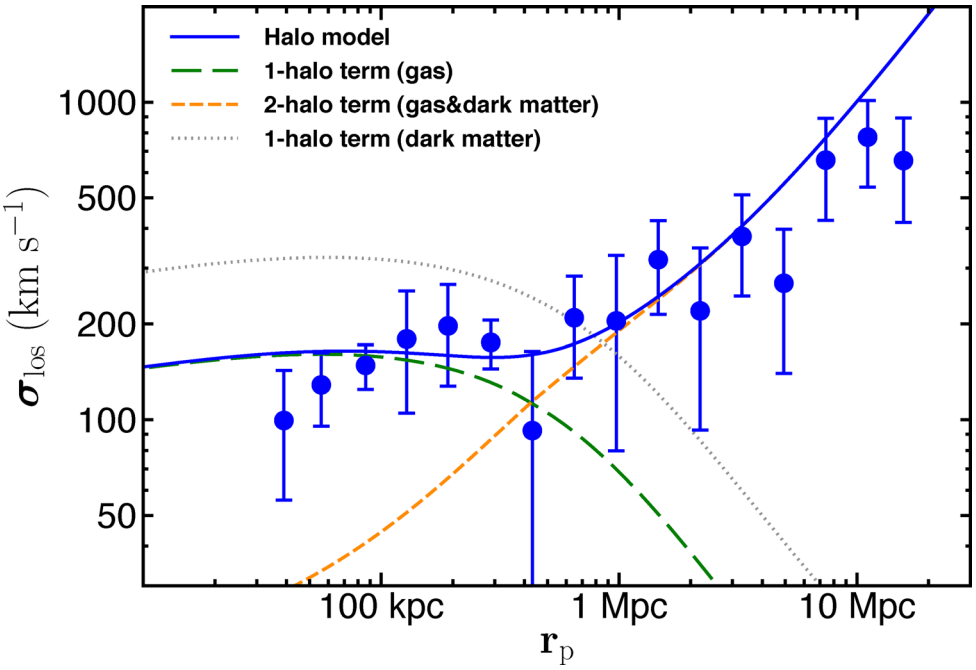

Figure 8. The velocity dispersion of gas clouds traced by Mg II absorption. The lines are the halo model decomposed into one-halo and two-halo terms. With the halo mass ($10^{13.5}$ M$_\odot$) fixed, there is only one free parameter in the model, the velocity bias $\mu \equiv \sigma_{\rm gas}/\sigma_{\rm m} \approx 1/2$.

dispersion of Mg II gas clouds increases from about 100 kms^{-1} at 30 kpc to about 700 kms^{-1} at 20 Mpc. We now use the halo model to investigate such spatial dependence of the gas cloud velocity dispersion. We fix the best fitting halo mass $M_{\rm halo} = 10^{13.5}\,{\rm M}_{\odot}$ and gas-to-mass ratios and constrain the motion of gas with respect to the predicted motion of collisionless dark matter.

As the surface density, the total line-of-sight velocity dispersion is decomposed into one-halo and two-halo terms:

$$\sigma^2_{\rm los}(r_{\rm p}|M) = \mu^2(M) A^{\rm 1h}(r_{\rm p}|M)\,\sigma^2_{\rm 1h,los}(r_{\rm p}|M) + A^{\rm 2h}(r_{\rm p}|M)\,\sigma^2_{\rm 2h,los}(r_{\rm p}|M), \quad (21)$$

where A is the mass contribution of each term:

$$A^{\rm 1h}(r_{\rm p}|M) = \frac{\Sigma^{\rm 1h}(r_{\rm p}|M)}{\Sigma^{\rm 1h}(r_{\rm p}|M) + \Sigma^{\rm 2h}(r_{\rm p}|M)},$$

$$A^{\rm 2h}(r_{\rm p}|M) = \frac{\Sigma^{\rm 2h}(r_{\rm p}|M)}{\Sigma^{\rm 1h}(r_{\rm p}|M) + \Sigma^{\rm 2h}(r_{\rm p}|M)}, \quad (22)$$

and $\mu \equiv \sigma_{\rm gas}/\sigma_{\rm m}$ is the velocity bias between gas and dark matter. Note $M_{\rm halo}$ is simplified to be M above.

On scales less than about 1 Mpc, the velocity dispersion is dominated by the motion of particles within the host halo. This one-halo term is obtained by solving Jeans equation of the NFW density profile for the virial motion of dark matter. On larger scales, the two-halo term is the width of redshift-space correlation function, determined by the statistics of peculiar velocities, which describe the relative motion of neighbouring haloes and of particles within them, with respect to the background comoving frame (i.e. the Hubble flow). We estimate each contribution in the standard linear theory. A detailed prescription of the halo model for velocity dispersion is presented in Appendix A2.

The halo model is presented with the observations in Fig. 8. On large scales, the velocity dispersion is dominated by the Hubble flow and varies roughly linearly with scale. The observed width of the Mg II absorption is in good agreement with the expectation from the theory of dark matter fluctuations, indicating the contributing gas clouds reside in neighbouring dark matter haloes. On small scales, we observe that the velocity dispersion of the Mg II gas clouds is smaller than the virial velocity dispersion of collisionless dark matter. This implies that Mg II clouds found within the virial radius of LRGs are gravitationally bound and will not escape. It also shows that these clouds do not trace satellite galaxies within the halo. Their slower motion might be due to the fact that they are subject to the pressure of the hot gas filling the halo.

To fully characterize the radial distribution of gas velocity dispersion, we fit the observational results with equation (22), using the best fitting halo mass derived above. We find the velocity bias μ to be about $1/2$, i.e. the gas cloud velocity dispersion around LRGs is a factor of 2 smaller than that of dark matter. Finally, we point out that, having previously estimated the mean halo mass of LRGs, a model having only one free parameter, the velocity bias μ, is able to fit the data across three orders of magnitude in scale.

6 SUMMARY

The phase-space distribution of baryons and in particular metals encodes key information on galaxy formation processes. Absorption line spectroscopy is a powerful tool to probe gaseous matter but on large scales around galaxies, where densities are low, the direct detection of absorber systems is challenging. In this paper, we use a statistical approach aimed at measuring absorption lines typically weaker than the noise level of individual background sources. We present a measurement of the mean Mg II $\lambda\lambda$2796, 2803 absorption around LRGs, based on cross-correlating the positions of about one million red galaxies at $z \sim 0.5$ and the flux decrements induced in the spectra of about 10^5 background quasars from the SDSS (see also Pérez-Ràfols et al., in preparation). We use quasar continuum estimates from Zhu & Ménard (2013a) with calibration improvements to remove large-scale, sub-percent variations. Our ability to measure the absorption signal over a broad range of scales allows us to interpret the phase-space distribution of the gas in a cosmological context. Our results are summarized as follows.

(i) We measure the LRG–Mg II correlation function from 30 kpc, where gas is associated with the LRG host halo, to about 20 Mpc, where it is dominated by contribution from neighbouring haloes. This galaxy–gas correlation reveals a change of slope on scales of about 1 Mpc, consistent with the expected transition from a dark matter halo dominated environment to a regime where clustering is dominated by halo–halo correlations. We use the observed rest equivalent width as a function of scale to obtain an estimate of the gas surface density, taking into account mild saturation effects on the smallest scales.

(ii) We find the standard halo model to provide an accurate description of the gas distribution over three orders of magnitude in scale under the simple assumption that the average distribution of Mg II gas follows that of dark matter up to a gas-to-mass ratio. Only three parameters are needed to describe the full range of measurements: the average host halo mass $M_{\rm halo}$, gas-to-mass ratio in the host halo $f^{\rm 1h}_{\rm Mg\,II}$, and mean gas-to-mass ratio in all neighbouring haloes $f^{\rm 2h}_{\rm halo}$. We find that a halo mass $M_{\rm halo} = 10^{13.5}\,{\rm M}_{\odot}$ provides an excellent fit to the data. This LRG host halo mass is in good agreement with the constraints from the galaxy–galaxy and galaxy–mass correlation functions. Moreover, we find $f^{\rm 1h}_{\rm halo}$ to be consistent with $f^{\rm 2h}_{\rm halo}$.

(iii) Combining observations of the galaxy–mass and galaxy–gas correlation functions we obtain *direct* constraints on the gas-to-mass ratio around LRGs $f^{\rm 1,2h}_{\rm halo}$ and find it to be roughly scale independent. This implies that (i) the average cool gas density profile around LRGs is consistent with the NFW profile, (ii) the density of Mg II clouds around LRGs is consistent with the cosmic value, estimated to be $\Omega^{\rm CGM}_{\rm Mg\,II} \approx 3 \times 10^{-9}$.

(iv) From linewidth estimates, we show that the velocity dispersion of the gas clouds also displays the expected one-halo and two-halo behaviours. On large scales the gas distribution follows the Hubble flow, whereas on small scales we observe the velocity dispersion of Mg II gas clouds to be lower than that of collisionless dark matter particles within their host halo, by a factor of about 2. This indicates that Mg II gas clouds are gravitationally bound to their host haloes and are likely falling towards the centre of the potential unless a pressure gradient is large enough to stop them.

These results provide us with a new set of constraints on the large-scale distribution of gas. Extending the analysis to other species and different types of galaxies will help understanding the cosmic baryon cycle.

Large and homogeneous surveys of the sky have allowed us to probe the distribution of matter in low-density environments. From the SDSS only, we now have measurements of the galaxy–galaxy correlation function from clustering analyses (e.g. Zehavi et al. 2005), the galaxy–mass correlation from gravitational lensing (e.g. Mandelbaum et al. 2006), the galaxy–dust correlation from reddening measurements (Ménard et al. 2010) and, from this paper, the

galaxy–gas correlation function obtained by measuring statistical absorption by metals. The velocity-space distribution of galaxies is also measured with various surveys (e.g. Jing, Mo & Boerner 1998; Conroy et al. 2007). Our work extends these measurements to one tracer of the gas distribution. These correlation functions are successfully interpreted in the standard CDM cosmological context and provide us with a more complete description of the matter distribution around galaxies in the phase space.

Our analysis demonstrates the power and potential of absorption line studies using the ever-growing data from large surveys. The methods we developed in Zhu & Ménard (2013a,b) and this paper are generic and readily applicable to any large data set from future surveys eBOSS (Comparat et al. 2013), BigBOSS (Schlegel et al. 2011), and PFS (Ellis et al. 2012). These surveys will provide large samples of different types of galaxies at higher redshift where more species are accessible from the ground and a golden opportunity to improve our understanding of the gas distribution and the cosmic baryon cycle. This work also shows that a detection of the baryon acoustic oscillation feature with Mg II absorption is within reach.

ACKNOWLEDGEMENTS

This work was supported by NSF Grant AST-1109665, the Alfred P. Sloan foundation and a grant from Theodore Dunham, Jr., Grant of Fund for Astrophysical Research. We thank Jordi Miralda-Escudé for useful discussions and comments on the manuscript. We also thank Daniel Eisenstein for useful discussions. We also thank an anonymous referee for useful comments that have helped improve the paper.

Funding for the SDSS and SDSS-II has been provided by the Alfred P. Sloan Foundation, the Participating Institutions, the National Science Foundation, the US Department of Energy, the National Aeronautics and Space Administration, the Japanese Monbukagakusho, the Max Planck Society, and the Higher Education Funding Council for England. The SDSS web site is http://www.sdss.org/. Funding for SDSS-III has been provided by the Alfred P. Sloan Foundation, the Participating Institutions, the National Science Foundation, and the US Department of Energy Office of Science. The SDSS-III web site is http://www.sdss3.org/.

SDSS-III is managed by the Astrophysical Research Consortium for the Participating Institutions of the SDSS-III Collaboration including the University of Arizona, the Brazilian Participation Group, Brookhaven National Laboratory, University of Cambridge, Carnegie Mellon University, University of Florida, the French Participation Group, the German Participation Group, Harvard University, the Instituto de Astrofisica de Canarias, the Michigan State/Notre Dame/JINA Participation Group, Johns Hopkins University, Lawrence Berkeley National Laboratory, Max Planck Institute for Astrophysics, Max Planck Institute for Extraterrestrial Physics, New Mexico State University, New York University, Ohio State University, Pennsylvania State University, University of Portsmouth, Princeton University, the Spanish Participation Group, University of Tokyo, University of Utah, Vanderbilt University, University of Virginia, University of Washington, and Yale University.

REFERENCES

Abazajian K. N. et al., 2009, ApJS, 182, 543
Asplund M., Grevesse N., Sauval A. J., Scott P., 2009, ARA&A, 47, 481
Bardeen J. M., Bond J. R., Kaiser N., Szalay A. S., 1986, ApJ, 304, 15
Bergeron J., 1986, A&A, 155, L8
Berlind A. A., Weinberg D. H., 2002, ApJ, 575, 587
Binney J., Tremaine S., 1987, Galactic Dynamics. Princeton Univ. Press, Princeton, NJ
Blanton M. R., Roweis S., 2007, AJ, 133, 734
Bolton A. S. et al., 2012, AJ, 144, 144
Bordoloi R. et al., 2011, ApJ, 743, 10
Bouché N., Murphy M. T., Péroux C., 2004, MNRAS, 354, L25
Bryan G. L., Norman M. L., 1998, ApJ, 495, 80
Bullock J. S., Kolatt T. S., Sigad Y., Somerville R. S., Kravtsov A. V., Klypin A. A., Primack J. R., Dekel A., 2001, MNRAS, 321, 559
Chen Y.-M. et al., 2012, MNRAS, 421, 314
Churchill C. W., Rigby J. R., Charlton J. C., Vogt S. S., 1999, ApJS, 120, 51
Churchill C. W., Mellon R. R., Charlton J. C., Jannuzi B. T., Kirhakos S., Steidel C. C., Schneider D. P., 2000, ApJS, 130, 91
Colín P., Klypin A. A., Kravtsov A. V., 2000, ApJ, 539, 561
Comparat J. et al., 2013, MNRAS, 428, 1498
Conroy C. et al., 2007, ApJ, 654, 153
Cooray A., Sheth R., 2002, Phys. Rep., 372, 1
Dawson K. S. et al., 2013, AJ, 145, 10
Diemand J., Moore B., Stadel J., 2004, MNRAS, 352, 535
Eisenstein D. J., Hu W., 1999, ApJ, 511, 5
Eisenstein D. J. et al., 2011, AJ, 142, 72
Ellis R. et al., 2012, preprint (arXiv:1206.0737)
Fisher K. B., 1995, ApJ, 448, 494
Gao L., Springel V., White S. D. M., 2005, MNRAS, 363, L66
Gauthier J.-R., Chen H.-W., Tinker J. L., 2009, ApJ, 702, 50
Gnedin N. Y., 2000, ApJ, 542, 535
Gorski K., 1988, ApJ, 332, L7
Gunn J. E. et al., 1998, AJ, 116, 3040
Gunn J. E. et al., 2006, AJ, 131, 2332
Hamilton A. J. S., 1992, ApJ, 385, L5
Hamilton A. J. S., Kumar P., Lu E., Matthews A., 1991, ApJ, 374, L1
Hewett P. C., Wild V., 2010, MNRAS, 405, 2302
Hu W., Kravtsov A. V., 2003, ApJ, 584, 702
Jing Y. P., Mo H. J., Boerner G., 1998, ApJ, 494, 1
Kaiser N., 1987, MNRAS, 227, 1
Kelleher D. E., Podobedova L. I., 2008, J. Phys. Chem. Ref. Data, 37, 267
Lee D. D., Seung H. S., 1999, Nature, 401, 788
Łokas E. L., Mamon G. A., 2001, MNRAS, 321, 155
Lundgren B. F. et al., 2009, ApJ, 698, 819
Lundgren B. F., Wake D. A., Padmanabhan N., Coil A., York D. G., 2011, MNRAS, 417, 304
Ma C.-P., Fry J. N., 2000, ApJ, 543, 503
Mandelbaum R., Tasitsiomi A., Seljak U., Kravtsov A. V., Wechsler R. H., 2005, MNRAS, 362, 1451
Mandelbaum R., Seljak U., Kauffmann G., Hirata C. M., Brinkmann J., 2006, MNRAS, 368, 715
Ménard B., Scranton R., Fukugita M., Richards G., 2010, MNRAS, 405, 1025
Mo H. J., Jing Y. P., Borner G., 1997, MNRAS, 286, 979
Morton D. C., 2003, ApJS, 149, 205
Narayanan A., Misawa T., Charlton J. C., Kim T.-S., 2007, ApJ, 660, 1093
Navarro J. F., Frenk C. S., White S. D. M., 1996, ApJ, 462, 563
Navarro J. F., Frenk C. S., White S. D. M., 1997, ApJ, 490, 493
Nestor D. B., Turnshek D. A., Rao S. M., 2005, ApJ, 628, 637
Okamoto T., Gao L., Theuns T., 2008, MNRAS, 390, 920
Oosterloo T. et al., 2010, MNRAS, 409, 500
Peacock J. A., Smith R. E., 2000, MNRAS, 318, 1144
Peebles P. J. E., 1980, The Large-scale Structure of the Universe. Princeton Univ. Press, Princeton, NJ
Press W. H., Schechter P., 1974, ApJ, 187, 425
Rees M. J., 1986, MNRAS, 218, 25p
Schlegel D. et al., 2011, preprint (arXiv:1106.1706)
Schneider D. P. et al., 2010, AJ, 139, 2360
Scoccimarro R., 2004, Phys. Rev. D, 70, 083007
Scoccimarro R., Sheth R. K., Hui L., Jain B., 2001, ApJ, 546, 20
Seljak U., 2000, MNRAS, 318, 203
Sheth R. K., Diaferio A., 2001, MNRAS, 322, 901

Sheth R. K., Tormen G., 1999, MNRAS, 308, 119
Sheth R. K., Mo H. J., Tormen G., 2001a, MNRAS, 323, 1
Sheth R. K., Hui L., Diaferio A., Scoccimarro R., 2001b, MNRAS, 325, 1288
Smee S. A. et al., 2013, AJ, 146, 32
Steidel C. C., Sargent W. L. W., 1992, ApJS, 80, 1
Steidel C. C., Erb D. K., Shapley A. E., Pettini M., Reddy N., Bogosavljević M., Rudie G. C., Rakic O., 2010, ApJ, 717, 289
Takada M., Jain B., 2003, MNRAS, 344, 857
Tinker J. L., Weinberg D. H., Zheng Z., Zehavi I., 2005, ApJ, 631, 41
Tumlinson J. et al., 2011, Science, 334, 948
Wechsler R. H., Zentner A. R., Bullock J. S., Kravtsov A. V., Allgood B., 2006, ApJ, 652, 71
Weinberg N. N., Kamionkowski M., 2003, MNRAS, 341, 251
White M. et al., 2011, ApJ, 728, 126
York D. G. et al., 2000, AJ, 120, 1579
Young L. M. et al., 2011, MNRAS, 414, 940
Zehavi I. et al., 2005, ApJ, 621, 22
Zhu G., Ménard B., 2013a, ApJ, 770, 130
Zhu G., Ménard B., 2013b, ApJ, 773, 16
Zhu G., Zheng Z., Lin W. P., Jing Y. P., Kang X., Gao L., 2006, ApJ, 639, L5

APPENDIX A: THE DARK MATTER–GAS HALO MODEL

A1 The projected surface density

The halo model (e.g. Ma & Fry 2000; Peacock & Smith 2000; Seljak 2000; Scoccimarro et al. 2001; Berlind & Weinberg 2002; Cooray & Sheth 2002, and references therein) provides a simple tool linking observations of the large-scale distribution of matter to theoretical predictions by dark matter cosmological models that is much less expensive than *N*-body/hydrodynamic simulations. It was originally developed to investigate the galaxy and dark matter distribution, we here extend its use to the galaxy–gas correlation function.

We start with the formal definition of the projected galaxy–gas correlation function (equation 2):

$$\omega_{\rm gal-gas}(r_{\rm p}) \equiv \langle \delta_{\rm gal}(r') \times \delta_{\rm gas}(r'+r_{\rm p})\rangle, \tag{A1}$$

where the ensemble average is performed over the entire area of interest. When the galaxy field is discretized, the ensemble average is restricted to the galaxy positions. The projected galaxy–gas correlation function is then equivalent to the *excess* of the surface density, given by equation (5), which we rewrite here:

$$\langle \Sigma_{\rm gas}(r_{\rm p})\rangle_{\rm gal} \equiv \overline{\Sigma}_{\rm gas}\, \omega_{\rm gal-gas}(r_{\rm p}). \tag{A2}$$

Below we will drop the ensemble symbol for simplicity.

In the halo model, we divide the surface density into one-halo and two-halo terms:

$$\Sigma_{\rm gas}(r_{\rm p}) = \Sigma^{\rm 1h}_{\rm gas}(r_{\rm p}) + \Sigma^{\rm 2h}_{\rm gas}(r_{\rm p}). \tag{A3}$$

For central galaxies, the one-halo term is obtained by integrating the host halo density profile along the line of sight and the two-halo term is computed through the cross-correlation function between the centre position of the host halo and gas in other haloes. For satellite galaxies, the one-halo term includes contribution from its own host (sub-)halo and its parent halo, and the two-halo term is again the contribution from neighbouring haloes. We assume all LRGs are central galaxies and will therefore only present the central-galaxy terms below. For an example of modelling the satellite contribution in the galaxy–mass correlation, we refer the reader to Mandelbaum et al. (2005).

The essential assumption of the dark matter halo model is that the properties (e.g., profile, density bias, abundance, galaxy occupation) of a dark matter halo are solely determined by its mass M (e.g. Press & Schechter 1974; Sheth & Tormen 1999). Though it has been shown recently that the formation history also plays an important role (the assembly bias, e.g. Gao, Springel & White 2005; Wechsler et al. 2006; Zhu et al. 2006), we ignore this subtlety here. To apply the halo model to the galaxy–gas correlation function, we further assume that the gas-to-mass ratio ($f_{\rm gas}$) depends only on the halo mass, and does not depend on scale, i.e. the shape of the density profile is the same for gas and dark matter. The halo model we use has three parameters:

(i) the average virial mass M of the host dark matter haloes,
(ii) the gas-to-mass ratio $f^{\rm 1h}_{\rm gas}(M)$ of the host dark matter haloes (the one-halo term),
(iii) the mean gas-to-mass ratio $f^{\rm 2h}_{\rm gas}$ of all galaxies at the same redshift (the two-halo term).

The mean excess of the gas surface density around galaxies then follows

$$\Sigma_{\rm gas}(r_{\rm p}|M) = f^{\rm 1h}_{\rm gas}(M)\, \Sigma^{\rm 1h}_{\rm m}(r_{\rm p}|M) + f^{\rm 2h}_{\rm gas}\, \Sigma^{\rm 2h}_{\rm m}(r_{\rm p}|M). \tag{A4}$$

We note that the two-halo term $f^{\rm 2h}_{\rm gas}$ is the mean value over all neighbouring haloes, which can have a wide range of gas-to-mass ratios.

We now present the ingredients for the one-halo and two-halo mass terms $\Sigma^{\rm 1h}_{\rm m}(r_{\rm p}|M)$ and $\Sigma^{\rm 2h}_{\rm m}(r_{\rm p}|M)$.

(i) *One-halo term*. The one-halo term is obtained by integrating the 3D density profile along the line of sight. We assume the dark matter density profile follows the NFW form (Navarro, Frenk & White 1996, 1997):

$$\rho_{\rm m}(r|M) = \frac{\rho_{\rm s}}{(r/r_{\rm s})^{\gamma}(1+r/r_{\rm s})^{3-\gamma}}, \tag{A5}$$

where $\gamma = 1$. We express the scale radius $r_{\rm s}$ in terms of concentration c and virial radius $r_{\rm vir}$: $r_{\rm s} = r_{\rm vir}/c$. The virial radius for a given halo mass M is determined through

$$M = \frac{4\pi}{3}\bar{\rho}_{\rm m}\Delta_{\rm vir} r^3_{\rm vir}, \tag{A6}$$

where $\bar{\rho}_{\rm m}$ is the mean matter density and $\Delta_{\rm vir}$ is the critical overdensity for virialization, for which we adopt the fitting formula by Bryan & Norman (1998):

$$\Delta_{\rm vir}(z) = \frac{1}{\Omega_{\rm m}(z)}\left\{18\pi^2 + 82\left[\Omega_{\rm m}(z) - 1\right] - 39\left[\Omega_{\rm m}(z) - 1\right]^2\right\}. \tag{A7}$$

We assume the concentration c follows

$$c(M, z) = \frac{c_0}{1+z}\left[\frac{M}{M_\star}\right]^{-\beta}. \tag{A8}$$

We take $c_0 = 9$ and $\beta = 0.13$ (e.g. Bullock et al. 2001; Hu & Kravtsov 2003). The non-linear scale mass $M_\star = 10^{12.7}\,{\rm M}_\odot$ for the adopted cosmology. The scale density $\rho_{\rm s}$ is then determined through the integration of the profile:

$$M = \int_0^{r_{\rm vir}} 4\pi r^2\,\rho_{\rm m}(r|M)\,{\rm d}r = \frac{4\pi\rho_{\rm s} r_{\rm vir}^3}{c^3}\left[\ln(1+c) - \frac{c}{1+c}\right], \tag{A9}$$

where the second equal sign holds only for the NFW slope $\gamma = 1$ (see Takada & Jain 2003 for analytic formulae for other profiles).
To obtain the surface density, we integrate the NFW density profile along the line of sight:

$$\Sigma_{\rm m}^{\rm 1h}(r_{\rm p}|M) = \int_{-\infty}^{+\infty} \rho_{\rm m}\left(\sqrt{r_{\rm p}^2 + s^2}|M\right)\,{\rm d}s. \tag{A10}$$

On large scales, the projected density profile follows $r_{\rm p}^{-2}$.

(ii) *Two-halo term.* The two-halo term is obtained by integrating the 3D cross-correlation function between the centre position of the halo and matter of neighbouring haloes $\xi_{\rm hm}$:

$$\Sigma_{\rm m}^{\rm 2h}(r_{\rm p}|M) = \bar{\rho}_{\rm m}\int_{-\infty}^{+\infty} \xi_{\rm hm}(\sqrt{r_{\rm p}^2 + s^2}|M)\,{\rm d}s. \tag{A11}$$

Note that we have again dropped the background term so that this is the *excess* of the surface density. The correlation function $\xi_{\rm hm}$ in the halo model involves convolution of the halo–halo correlation function and the halo density profile. Since convolution in real space is simply multiplication in Fourier space, it is easier to calculate the power spectrum $P_{\rm hm}(k)$ first then obtain the correlation function by Fourier Transformation. The two-halo power spectrum is given by

$$P_{\rm hm}(k) = b(M)P_{\rm lin}(k)\int_{M_{\rm min}}^{M_{\rm max}} {\rm d}\nu\, f_\nu b(\nu)u(k|\nu), \tag{A12}$$

where we have followed the convention and used the overdensity peak height ν (e.g. Bardeen et al. 1986):

$$\nu \equiv \frac{\delta_c(z)}{D(z)\sigma(M)}. \tag{A13}$$

Here, $D(z)$ is the growth factor and $\delta_c(z)$ is the overdensity threshold for spherical collapse, for which we use the fitting formula given by Weinberg & Kamionkowski (2003):

$$\delta_{\rm c}(z) = \frac{3}{20}(12\pi)^{2/3}\left[1 + 0.013\log_{10}\Omega_{\rm m}(z)\right]. \tag{A14}$$

The $\sigma(M)$ term is the present-day rms fluctuation in the mass density, smoothed with a top-hat filter of radius $R(M) \equiv (3M/4\pi\bar{\rho}_{\rm m})^{1/3}$:

$$\sigma^2(M) = \int_0^{+\infty}\frac{{\rm d}k}{k}\frac{k^3 P_{\rm lin}(k)}{2\pi^2}W^2(kR), \tag{A15}$$

where W is the Fourier transform of the top-hat window function:

$$W(x) = \frac{3}{x^3}(\sin x - x\cos x). \tag{A16}$$

For the large-scale bias b, we use the fitting formula:

$$b(M, z) = b(\nu) = 1 + \frac{1}{\sqrt{a}\delta_{\rm c}}\left[\sqrt{a}(a\nu^2) + \sqrt{a}b(a\nu^2)^{1-c} - \frac{(a\nu^2)^c}{(a\nu^2)^c + b(1-c)(1-c/2)}\right], \tag{A17}$$

with $a = 1/\sqrt{2}$, $b = 0.35$, and $c = 0.8$ (Sheth, Mo & Tormen 2001a; Tinker et al. 2005). The mass function $f(\nu)$ is defined as

$$\frac{{\rm d}n}{{\rm d}M}{\rm d}M = \frac{\bar{\rho}_{\rm m}}{M}f(\nu){\rm d}\nu, \tag{A18}$$

and we use the fitting formula given by Sheth & Tormen (1999):

$$\nu f(\nu) = A\sqrt{\frac{2a\nu^2}{\pi}}\left[1 + (a\nu^2)^{-p}\right]\exp\left(-\frac{a\nu^2}{2}\right), \tag{A19}$$

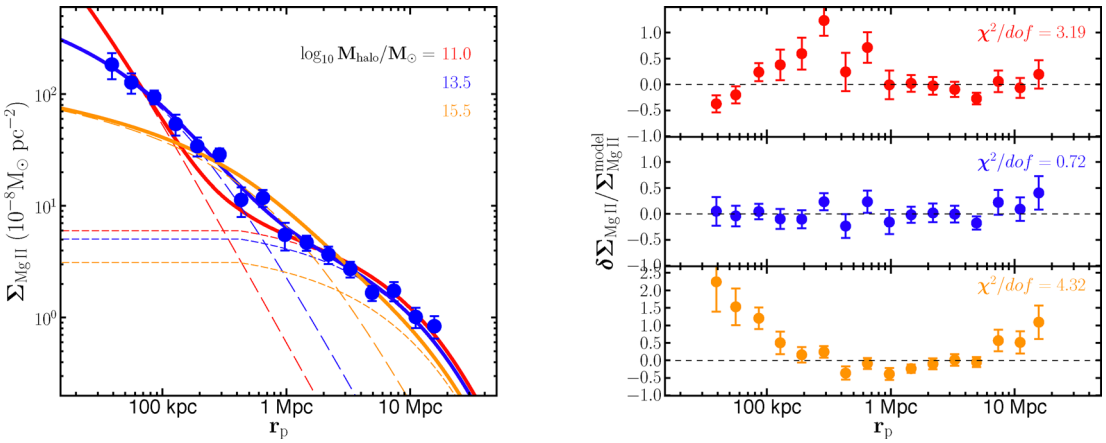

Figure A1. The best fitting halo models (left-hand panel) and fractional residuals (right-hand panel) for three halo masses: $10^{11}\,M_\odot$, $10^{13.5}$ (the best fitting mass) and $10^{15.5}\,M_\odot$. The best fitting Mg II gas-to-mass ratios are $(\log_{10} f_{gas}^{1h}, \log_{10} f_{gas}^{2h}) = (-6.2, -7.6)$, $(-8.3, -8.1)$ and $(-9.6, -9.1)$, respectively. The line styles are the same as in Fig. 5, with different colours representing different masses.

with $a = 0.707$ and $p = 0.3$. The coefficient A is set by the normalization condition:

$$\int_0^{+\infty} f(\nu)\mathrm{d}\nu = 1, \tag{A20}$$

and is 0.129 in the cosmology we adopted. The $u(k|\nu)$ term is the Fourier transform of the density profile:

$$u(k|\nu) = \int 4\pi r^2 \mathrm{d}r\ \rho(r|M)\frac{\sin kr}{kr}. \tag{A21}$$

For the linear power spectrum $P_{lin}(k)$, we use the fitting formula given by Eisenstein & Hu (1999). Note that the power spectrum is given in comoving space and after the Fourier transformation we convert the correlation function into physical space.

The integral of the halo-mass power spectrum (equation A12) is performed from $M_{min} = 10^3\,M_\odot$ to $M_{max} = 10^{17}\,M_\odot$. On large scales, the integral must equal 1, so we also scale the integral such that it satisfies this condition. For metals, there is a lower halo-mass limit below which no stars can form and metals can only come from stars formed in other haloes (Rees 1986). It is yet unknown what this lower limit is (e.g. Gnedin 2000; Okamoto, Gao & Theuns 2008), but it only affects the overall amplitude of the integral, which we force to be one on large scales, so we keep $M_{min} = 10^3\,M_\odot$. The upper limit could be adjusted to take into account the halo exclusion effect, which only affects the small-scale power where the one-halo term dominates, so we keep $M_{max} = 10^{17}\,M_\odot$.

Fig. A1 shows examples of halo models with different halo masses, with the best fitting Mg II gas-to-mass ratios determined by minimizing the chi-square. For $M = 10^{11}\,M_\odot$, the lowest mass we probe, the profile is too steep on small scales and cannot capture the transition between the one-halo and the two-halo terms. For $M = 10^{15.5}\,M_\odot$, the largest mass we probe, the profile is too flat on small scales. The best fitting halo mass, $M = 10^{13.5}\,M_\odot$, provides an excellent fit to the measurements.

A2 The line-of-sight velocity dispersion

The total line-of-sight velocity dispersion of particles around a halo with mass M is the mass-weighted summation, in quadrature, of the velocity dispersion of all particles along the line of sight:

$$\sigma^2_{los}(r_p|M) = \frac{1}{\Sigma(r_p|M)}\int_{-\infty}^{+\infty} \rho_m\left(\sqrt{r_p^2+s^2}|M\right)\sigma^2_{los}(r_p, s)\,\mathrm{d}s, \tag{A22}$$

where the line-of-sight dispersion at a given separation (r_p, s) is given by combining the radial $(\sigma_\parallel)$ and tangential $(\sigma_\perp)$ dispersions:

$$\sigma^2_{los}(r_p, s) = \sigma^2_\parallel\left(\sqrt{r_p^2+s^2}\right)\sin^2\theta + \frac{1}{2}\sigma^2_\perp\left(\sqrt{r_p^2+s^2}\right)\cos^2\theta, \tag{A23}$$

with θ being the angle between the projection direction and the 3D separation, i.e. $\theta = \arctan(s/r_p)$. The radial $(\sigma_\parallel)$ and tangential $(\sigma_\perp)$ velocity dispersions are related by the velocity anisotropy:

$$\beta = 1 - \frac{\sigma^2_\perp}{2\sigma^2_\parallel}. \tag{A24}$$

The integral can be rewritten as

$$\sigma^2_{\rm los}(r_{\rm p}|M) = \frac{1}{\Sigma(r_{\rm p}|M)} \int_{-\infty}^{+\infty} \rho_{\rm m}\left(\sqrt{r_{\rm p}^2+s^2}|M\right)\left(1-\beta\frac{r_{\rm p}^2}{r_{\rm p}^2+s^2}\right)\sigma^2_{\parallel}\left(\sqrt{r_{\rm p}^2+s^2}\right)\,{\rm d}s. \tag{A25}$$

We assume velocity isotropy, i.e. $\beta = 0$, throughout this analysis.

We decompose the total line-of-sight velocity dispersion into one-halo and two-halo terms, as for the surface density:

$$\sigma^2_{\rm los}(r_{\rm p}|M) = \mu^2(M)A^{\rm 1h}(r_{\rm p}|M)\,\sigma^2_{\rm 1h,los}(r_{\rm p}|M) + A^{\rm 2h}(r_{\rm p}|M)\,\sigma^2_{\rm 2h,los}(r_{\rm p}|M), \tag{A26}$$

where A is the mass contribution of each term:

$$A^{\rm 1h}(r_{\rm p}|M) = \frac{\Sigma^{\rm 1h}(r_{\rm p}|M)}{\Sigma^{\rm 1h}(r_{\rm p}|M)+\Sigma^{\rm 2h}(r_{\rm p}|M)}\,,\ A^{\rm 2h}(r_{\rm p}|M) = \frac{\Sigma^{\rm 2h}(r_{\rm p}|M)}{\Sigma^{\rm 1h}(r_{\rm p}|M)+\Sigma^{\rm 2h}(r_{\rm p}|M)}\,, \tag{A27}$$

and $\mu \equiv \sigma_{\rm gas}/\sigma_{\rm m}$ is the velocity bias between gas and dark matter.

(i) *One-halo term*. The one-halo term $\sigma^2_{\rm 1h}$ is obtained by solving Jeans equation (Binney & Tremaine 1987):

$$\frac{{\rm d}\sigma^2_{\parallel}(r)\rho(r)}{{\rm d}r} + \frac{2\beta(r)}{r}\sigma^2_{\parallel}(r)\rho(r) = -\rho(r)\frac{{\rm d}\phi}{{\rm d}r} = -\rho(r)\frac{GM(<r)}{r^2}. \tag{A28}$$

For NFW profile and constant velocity anisotropy β, Łokas & Mamon (2001) provides analytic solutions to the Jeans equation (equations 13–16 in their paper). The velocity anisotropy has been shown to weakly depend on scale, increasing from around 0.15 at small radius to about 0.4 at virial radius (Colín, Klypin & Kravtsov 2000; Diemand, Moore & Stadel 2004). The small anisotropy has little effect on the final line-of-sight velocity dispersion, so we assume velocity isotropy ($\beta = 0$), in which case the radial velocity dispersion is given by equation 14 in Łokas & Mamon (2001):

$$\sigma^2_{\parallel}(x) = \frac{1}{2}V^2_{\rm vir}\,g(c)cx(1+x)^2\left[\pi^2 - \log x - \frac{1}{x} - \frac{1}{(1+x)^2} - \frac{6}{1+x}\right.$$
$$\left. + \left(1+\frac{1}{x^2}-\frac{4}{x}-\frac{2}{1+x}\right)\log(1+x) + 3\log^2(1+x) - 6{\rm Li}_2(1+x)\right], \tag{A29}$$

where $x \equiv r/r_{\rm s} = cr/r_{\rm vir}$, c is the concentration, $V_{\rm vir}$ is the circular velocity at virial radius:

$$V_{\rm vir} = \sqrt{\frac{GM_{\rm vir}}{r_{\rm vir}}}, \tag{A30}$$

and

$$g(c) = \frac{1}{\log(1+c) - c/(1+c)}, \tag{A31}$$

and ${\rm Li}_2$ is the dilogarithm:

$${\rm Li}_2(z) = \int_1^z \frac{\log t}{1-t}{\rm d}t. \tag{A32}$$

The one-halo term of the line-of-sight velocity dispersion can then be obtained by integrating equation (A25). As we discussed in the main text, around LRGs this collisionless dark matter velocity dispersion is larger than the observed *gas cloud* velocity dispersion by about a factor of 2, i.e. $\mu_{\rm LRG} \approx 1/2$.

(ii) *Two-halo term*. The two-halo term $\sigma^2_{\rm 2h}$ is the width of the correlation function in the redshift (velocity) space, and is determined by two factors: (1) the relative motion of the neighbouring haloes with respect to the host halo (Peebles 1980; Hamilton et al. 1991; Mo, Jing & Borner 1997; Sheth & Diaferio 2001; Sheth et al. 2001b) and of particles within these neighbouring haloes, with respect to the background comoving frame; (2) the Hubble flow with peculiar velocity, which determines the Kaiser limit of the redshift-space correlation function (e.g. Kaiser 1987; Hamilton 1992). We present these two terms separately below. Alternatively, one can also fold the relative motion of haloes with respect to the background (the first term) into the Kaiser-limit redshift-space correlation function (e.g. Fisher 1995; Scoccimarro 2004).

We first present the prescription of the first term. The velocity dispersion between the centre of the host halo with mass M and gas in another halo with mass m at a distance r (in 3D) can be decomposed into four terms:

$$\sigma^2_{Mm}(r) = \sigma^2_{\rm halo}(M) + \sigma^2_{\rm halo}(m) + \mu^2(m)\sigma^2_{\rm vir}(m) - 2\Psi_{Mm}(r), \tag{A33}$$

where $\sigma_{\rm halo}(m)$ is the cosmic velocity dispersion of haloes with mass m, $\sigma_{\rm vir}(m)$ is the mean virial motion of particles within the halo, which can be obtained by solving the Jeans equation and taking the mass-weighted average, $\mu(m)$ is the velocity bias between gas and dark matter, and $\Psi_{Mm}(r)$ is the velocity correlation between two haloes because their velocities are not independent. For the two-halo term, we assume $\mu(m)$ to be 1, but it has little effect since the virial motion of particles plays a sub-dominant role on scales where two-halo term dominates.

Following Sheth & Diaferio (2001), the halo velocity dispersion from linear theory is given by

$$\sigma_{\rm halo}(m) = H_0 f(\Omega_{\rm m})\sigma_{-1}\sqrt{1-\sigma_0^4/\sigma_1^2\sigma_{-1}^2}, \tag{A34}$$

where $f(\Omega_{\rm m}) = {\rm d}\log D/\log a \approx \Omega_{\rm m}^{0.55}$ and

$$\sigma_j^2(m) = \frac{1}{2\pi^2}\int {\rm d}k\, k^{2+2j} P(k) W^2[kR(m)], \tag{A35}$$

with $W(x)$ being the Fourier transform of the top-hat smoothing window, as equation (A16). The square root term is to correct the fact that overdensities are not completely random patches. For $\Omega_{\rm m} \sim 0.3$, the halo velocity dispersion depends only weakly on mass and we use the fitting formula given by Sheth & Diaferio (2001):

$$\sigma_{\rm halo}(m) = \frac{\sigma_{\rm fit}}{1+(R/R_{\rm fit})^{\eta}}. \tag{A36}$$

For the adopted cosmology and at redshift $z = 0.52$, we find $R_{\rm fit} = 50$ Mpc, and $\eta = 0.85$, and $\sigma_{\rm fit} = 400\,{\rm kms}^{-1}$ provide a good fit.

The velocity correlation function from linear theory is given by Gorski (1988) and Sheth et al. (2001b):

$$\Psi_{Mm,\parallel/\perp}(r) = [H_0 f(\Omega_{\rm m})]^2\,(1-\sigma_0^4/\sigma_1^2\sigma_{-1}^2)\,\frac{1}{2\pi^2}\int {\rm d}k\, P(k) W[kR(M)] W[kR(m)] K_{\parallel/\perp}(kr), \tag{A37}$$

where for the radial ($\Psi_{Mm,\parallel}$) and tangential ($\Psi_{Mm,\perp}$) velocity correlations,

$$K_{\parallel}(x) = \frac{\sin x}{x} - \frac{2}{x^3}(\sin x - x\cos x)\,,\ K_{\perp}(x) = \frac{2}{x^3}(\sin x - x\cos x), \tag{A38}$$

respectively. The total velocity correlation is $\Psi_{Mm}(r) = \Psi_{Mm,\parallel}(r) + \Psi_{Mm,\perp}(r)$ and can be obtained by simply replacing $K_{\parallel/\perp}(x)$ with $K(x) = \sin x/x$.

To compute the total 3D velocity dispersion with respect to the host halo, we need to integrate σ_{Mm}^2 over all neighbouring haloes:

$$\sigma_{\rm 2h,3D}^2(r|M) = \frac{\int {\rm d}m\, n(m) m\,[1+\xi_{Mm}(r)]\,\sigma_{Mm}^2(r)}{\int {\rm d}m\, n(m) m\,[1+\xi_{Mm}(r)]}. \tag{A39}$$

The line-of-sight velocity dispersion, ignoring the Hubble flow for the time being, is then obtained by inserting this quantity into the integral A25:

$$\sigma_{\rm no\ Hubble}^2(r_{\rm p}|M) = \frac{1}{\Sigma^{\rm 2h}(r_{\rm p}|M)}\,\bar{\rho}_{\rm m}\int_{-\infty}^{+\infty} \xi_{\rm hm}\left(\sqrt{r_{\rm p}^2+s^2}|M\right)\frac{1}{3}\,\sigma_{\rm 2h,3D}^2\left(\sqrt{r_{\rm p}^2+s^2}|M\right){\rm d}s, \tag{A40}$$

where we have assumed velocity isotropy ($\beta = 0$). This equation involves a quadruple integral, one over m, one over k for σ_j^2, another over k for ξ, and one over r along the line of sight at $r_{\rm p}$. In practice, we find that choosing a typical neighbouring halo mass without doing the integral over m can provide a good approximation, and tests show that the results are insensitive to the chosen halo mass between 10^{10} and $10^{14}\,{\rm M}_\odot$. This is because the halo velocity dispersion only weakly depends on mass, and the presence of the velocity correlation further cancels out most of the dependence. We therefore use a typical halo mass $10^{12}\,{\rm M}_\odot$ to circumvent the computational difficulty and do not perform the integral over m.

We now turn to the second term, the width of the Kaiser-limit redshift-space correlation function along the line of sight. We estimate this term by measuring the full width at half-maximum (FWHM) and dividing it by 2.35, i.e. $\Delta v = {\rm FWHM}/2.35$. We model the correlation function with the standard spherical Legendre expansion method (Kaiser 1987; Hamilton 1992), and empirically determine the width of its line-of-sight projection as a function of impact parameter. For the adopted cosmology, at redshift $z = 0.5$, we find the following linear relation is a good approximation for the velocity width (FWHM/2.35):

$$\Delta v(r_{\rm p}) \approx 90\,{\rm kms}^{-1}\,\frac{r_{\rm p}}{\rm Mpc} + 100\,{\rm kms}^{-1}. \tag{A41}$$

This approximation is valid between about 1 and 20 Mpc but over-estimates the width beyond 20 Mpc. We do not go beyond 20 Mpc in this analysis.

The final two-halo term of the velocity dispersion is then given by

$$\sigma_{\rm 2h,los}^2(r_{\rm p}|M) = [\Delta v(r_{\rm p})]^2 + \sigma_{\rm no\,Hubble}^2(r_{\rm p}|M). \tag{A42}$$

APPENDIX B: SATURATION EFFECTS

In Section 5, we adopt line ratio 1.75 when $\langle W_0^{\rm Mg\,II}\rangle < 0.15$ Å, and equation (15) otherwise, as suggested by the median line ratios of individual Mg II absorbers. We then convert the rest equivalent width of the weaker line (λ2803) to the Mg II surface density. We here investigate two different extreme line ratio treatments: (1) line ratio equals 1 across all scales, i.e. the contributing absorption is all saturated; (2) line ratio equals 2 at $\langle W_0^{\rm Mg\,II}\rangle < 0.15$ Å, and 1 otherwise, i.e., the contributing absorption is all unsaturated at $\langle W_0^{\rm Mg\,II}\rangle < 0.15$ Å, and all saturated otherwise.

The best fitting halo models with these two line ratio treatments are presented in Fig. B1. The joint likelihood distributions are shown in Fig. B2. For comparison, we have also overplotted the same vertical grey and horizontal light blue bands as in Fig. 6, the constraints from the galaxy-mass correlation. The best fitting halo parameters shift by about 0.2–0.5 dex (1–2σ), showing these extreme line ratio treatments do not have a significant effect on our conclusions.

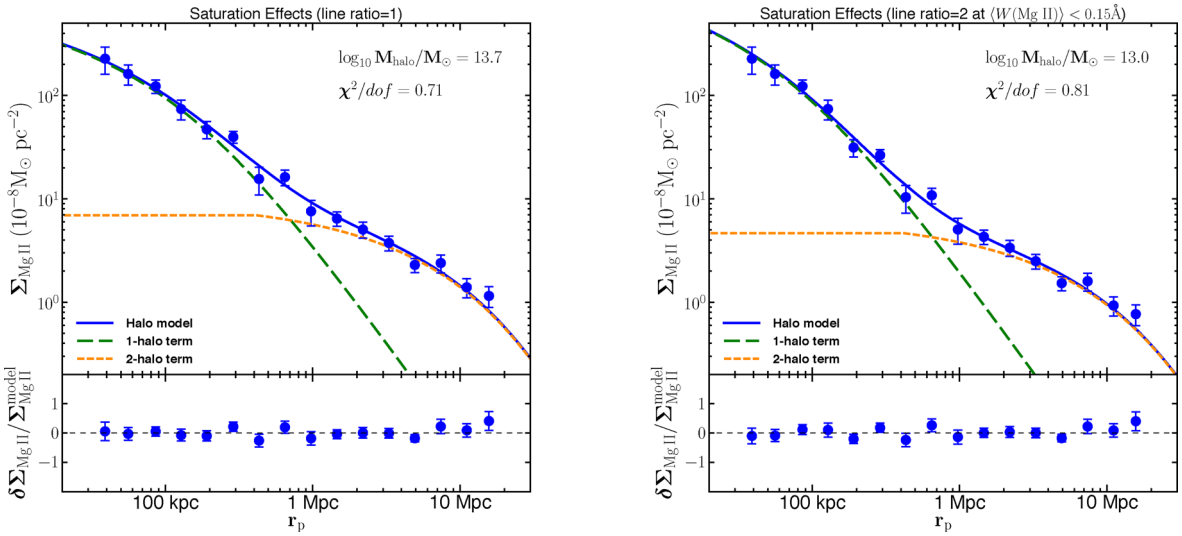

Figure B1. Saturation effects on column density and halo modelling. The left-hand panel shows the best fitting halo model if we adopt line ratio 1 everywhere. The right-hand panel shows the best fitting halo model if we adopt line ratio 2 when $\langle W_0^{\rm Mg\,II}\rangle < 0.15$ Å, and 1 otherwise.

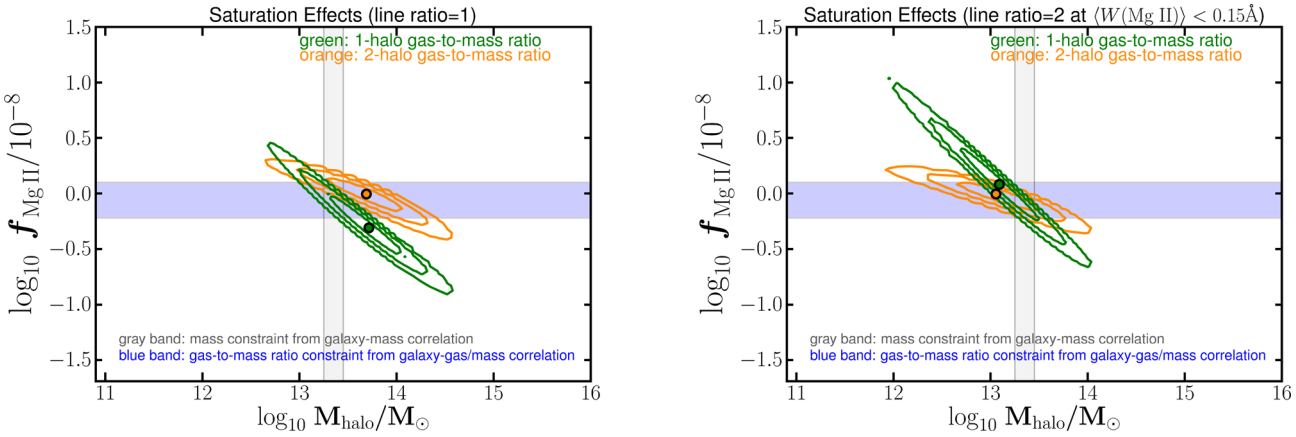

Figure B2. Joint likelihood distributions of halo mass and gas-to-mass ratios for different line ratio treatments. The vertical grey band and horizontal blue band are the same as in Fig. 6.

It is worth pointing out that what we measure is the *minimum* surface density because a fraction of the contributing absorbers must be saturated, even though accurate line ratio measurement and the choice of the weaker line can offer an estimate close to the true surface density. The saturation effect may become a major uncertainty when studying CGM of star-forming galaxies where we expect higher gas density (Bordoloi et al. 2011; Tumlinson et al. 2011; Zhu & Ménard 2013b). It is therefore necessary to develop more sophisticated models to include not only column density, but also Doppler broadening factor, covering fraction and other physical properties.

This paper has been typeset from a TEX/LATEX file prepared by the author.